

# Aerosp 481 Team 03: Libellula CDR Report



## Authors:

Niko Economos  
Shaylin Ciaramitaro  
Joon Kyo Kim  
Juan Esteban Vega  
Vienna Chafart  
Victoria Cobb

*University of Michigan Department of Aerospace Engineering*

# Contents

<b>1</b>	<b>Summary</b>	<b>4</b>
1.1	Executive Summary . . . . .	4
1.2	3D Design View . . . . .	5
1.3	Performance Parameters . . . . .	7
<b>2</b>	<b>Introduction</b>	<b>8</b>
<b>3</b>	<b>Considerations for Remote Piloting</b>	<b>9</b>
<b>4</b>	<b>Configuration</b>	<b>11</b>
<b>5</b>	<b>Preliminary Sizing</b>	<b>12</b>
5.1	Initial Weight Estimate . . . . .	13
5.2	T/W vs W/S . . . . .	13
5.3	Improved Weight Estimate . . . . .	15
5.4	$T$ vs $S$ with objective function . . . . .	15
<b>6</b>	<b>Interior Layout</b>	<b>17</b>
6.1	Fuselage . . . . .	17
6.2	Interior Components . . . . .	17
<b>7</b>	<b>Component Weight Breakdown</b>	<b>19</b>
7.1	Center of Gravity and Aircraft Balance . . . . .	21
<b>8</b>	<b>Stability and Control</b>	<b>22</b>
<b>9</b>	<b>Aerodynamics</b>	<b>25</b>
9.1	Wing Design . . . . .	25
9.1.1	Wing Area . . . . .	25
9.1.2	Aspect Ratio . . . . .	25
9.1.3	Span . . . . .	26
9.1.4	Taper Ratio . . . . .	26
9.1.5	Wing Incidence And Twist . . . . .	27
9.1.6	Sweep . . . . .	27
9.1.7	Wing Configuration . . . . .	28
9.1.8	High Lift Devices . . . . .	28
9.2	Wing Airfoil Selection . . . . .	30
9.3	Stall Speed . . . . .	31
9.4	Empennage Configuration . . . . .	32
9.4.1	Vertical Tail . . . . .	32
9.4.2	Horizontal Tail . . . . .	32
9.5	Empennage Airfoil Selection . . . . .	33
9.5.1	Vertical Tail . . . . .	33
9.5.2	Horizontal Tail . . . . .	34
9.6	Dimensions After Volume Coefficient Based Sizing and Airfoil Selection . . . . .	34
9.7	Refined Drag Estimates . . . . .	34
<b>10</b>	<b>Objective Function</b>	<b>35</b>
10.1	RTD&E and Flyaway Cost . . . . .	36
10.2	Operating Cost . . . . .	38
<b>11</b>	<b>Propulsion System</b>	<b>40</b>

<b>12 Government Furnished Equipment</b>	<b>41</b>
<b>13 Landing Gear</b>	<b>44</b>
13.1 Sizing . . . . .	44
13.2 Landing Gear Choice . . . . .	45
13.3 Integration . . . . .	46
<b>14 Design Refinement</b>	<b>46</b>
14.1 Engine Inlet Design . . . . .	47
14.2 Blended-wing Design . . . . .	47
14.3 Internal vs External Carriage . . . . .	47
14.4 Missile Reserves . . . . .	47
<b>15 Structures</b>	<b>48</b>
15.1 Load Paths . . . . .	48
15.1.1 Distribution of Air Loads on Wing . . . . .	49
15.2 V-n Diagrams . . . . .	50
15.2.1 Maneuverability . . . . .	50
<b>16 Computational Procedure and Software Design</b>	<b>51</b>
16.1 Initial Sizing . . . . .	52
16.2 Finding T, S, and Updated TOGW Estimate . . . . .	53
16.3 Iteration and Refinement . . . . .	54
16.4 Post Processing . . . . .	55
<b>17 Method Validation</b>	<b>55</b>
<b>18 Conclusions</b>	<b>56</b>
<b>19 References</b>	<b>57</b>
<b>20 Appendix</b>	<b>59</b>
20.1 Cost . . . . .	59
20.1.1 Adjusting for Inflation . . . . .	59
20.1.2 95% Learning Curve Correction . . . . .	59
20.2 Constraint Equations . . . . .	59
20.2.1 $\frac{W}{S}$ Constraint from Landing Field Length . . . . .	59
20.2.2 $\frac{T}{W}$ Takeoff Field Length . . . . .	59
20.2.3 $\frac{W}{S}$ Instantaneous Turn . . . . .	59
20.2.4 $\frac{T}{W}$ Sustained Turn . . . . .	60
20.2.5 $\frac{T}{W}$ Cruise and Dash . . . . .	60
20.2.6 $\frac{T}{W}$ Ceiling . . . . .	60
20.2.7 $\frac{T}{W}$ Climb . . . . .	60
20.2.8 $\frac{T}{W}$ Specific Excess Power . . . . .	61
20.3 Additional Equations . . . . .	61
20.3.1 Empty Weight Fraction Regression . . . . .	61
20.3.2 $S_{wet}$ from TOGW Regression . . . . .	61
20.4 Additional Plots . . . . .	62
20.5 Wing Parameters . . . . .	63
20.6 Wing Design . . . . .	64
20.7 Empennage Design . . . . .	68

# 1 Summary

## 1.1 Executive Summary

With increasing tensions across the globe, the AIAA has launched an Undergraduate Team Design Challenge to design an aircraft that meets these emerging security concerns. The design is to be a homeland defense interceptor, capable of completing three specified missions. Key requirements include a cost cap of \$25M per aircraft for a 1000 unit purchase and readiness for operational deployment by 2027.

The aircraft design prioritizes mission success by incorporating features that enhance speed, maneuverability, and stealth. The proposed interceptor features a single engine, highly swept back wing, and a single tail configuration to optimize aerodynamic performance. The design also features remote pilot capabilities to reduce cost and eliminate the weight associated with crew and life support systems, while also taking into account safety concerns that may have arose with a piloted aircraft.

The fuselage is designed to optimize aerodynamic efficiency, stealth, and internal capacity. It features a rounded nose, which minimizes drag and improving overall aerodynamic performance. An internal weapons bay is integrated into the fuselage, allowing for munitions to be carried without compromising the stealth of the aircraft during missions. This configuration also helps reduces the external drag typically associated with missiles mounted on wing launchers. The single engine design enables a more compact fuselage configuration, reducing weight and contributing to a large  $T/W$  ratio. The internal volume was maximized in this design in order to allow for advanced avionics, fuel storage, ammunition, and other mission-specified equipment.

The wing is designed to optimize the maneuverability, efficiency, and structural integrity of the aircraft. It features a highly swept-back wing configuration to reduce wave drag at transonic speeds. The mid-wing configuration minimizes interference drag, enhances performance at high G's and rapid maneuvers, and avoids ground clearance issues faced by low-wing designs and roll over-stability faced by high-wing designs. The wing utilizes a custom airfoil that was optimized through Mach Aero. For high lift devices, we are incorporating leading edge extensions, flaperons, and leading edge flaps. These features aim to simplify the overall design, thus reducing cost and weight, while also increasing the lift generated.

The empennage is designed to provide stability, control, and stealth, with a configuration that enhances the aircraft's overall aerodynamic performance. It features a single-tail design, which simplifies the structural layout while maintaining effective control authority. This configuration optimizes yaw and pitch control, contributing to streamlined flight dynamics and reducing developmental costs by minimizing the complexity of testing and manufacturing. The vertical tail is strategically positioned to minimize aerodynamic interference from the wings and fuselage, ensuring reliable handling and stability across all flight conditions, particularly during aggressive maneuvers or low-speed operations.

While this design has reached maturity for this stage of design, significant work remains before it can proceed to manufacturing and operational deployment. Our immediate next steps include refining our current design and preparing for the detailed design phase. Key actions include re-evaluating the selected airfoil for the wings, and the refinement and CAD integration of the leading edge extensions. Additionally, we will focus on iterative testing to identify further areas for improvement.

Ultimately, our aircraft design represents a significant advancement in homeland defense capabilities, aligning with the specified requirements of the AIAA Undergraduate Team Design Challenge. By integrating cutting-edge technologies and prioritizing aerodynamic efficiency, stealth, and operational flexibility, we are poised to deliver a high-performance interceptor that meets both budgetary and timeline constraints given within the competition requirements. As we progress into the detailed design phase, our focus will remain on iterative refinement and validation, ensuring that we achieve the highest standards of performance and safety. We are striving to create a system that not only fulfills its intended missions, but also sets a new benchmark for future military aircraft designs.

## 1.2 3D Design View

A Three-view drawing and perspective view of our aircraft is shown in the figure below. The views indicate the general dimensions of the aircraft, the center of gravity and neutral point, locations for control surfaces, and weapon stowage. In consideration of the neutral point, the derivation of which is discussed in the Stability and Control Section 8, different Mach numbers were considered; in this section, the fully-loaded condition at cruise ( $M = 0.85$ ) and the fully-expended condition at landing ( $M = 0.28$ ) will be discussed. The center of gravity was calculated to be around 9.236 m aft of the tip of the nose in the fully loaded condition. At cruise, the neutral point sits just after this point, at around 9.553 m aft of the nose tip. This places our loaded aircraft at a static margin of 13.6%, a region of moderate stability; although this exceeds the bounds of  $\pm 10\%$  in the static margin, our aircraft will possibly benefit more from being slightly more stable at takeoff to ensure a successful takeoff sequence and to prevent premature stall.

Also indicated in the drawings are the finalized landing gear positions and assemblies, which place the aircraft around 1 meter off the ground. The landing gear constraint angles are outlined in Table 1, using the most constraining CG location:

Table 1: Landing Gear Constraint Angles (Most Constrained)

Parameter for Loaded Aircraft	Value
Rotation Angle Clearance	11.84°
Tipback Angle	12.61°
Tipover Angle Clearance	27.75°
Overtake Angle	42.04°

The rotation clearance and tipback angles may seem low, but as discussed in later sections, it was found that a rotation angle of 10 degrees was sufficient for normal takeoff, thus our angles are satisfactory. The overtake angle is also satisfactory according to the absolute maximum constraint of 60 degrees.

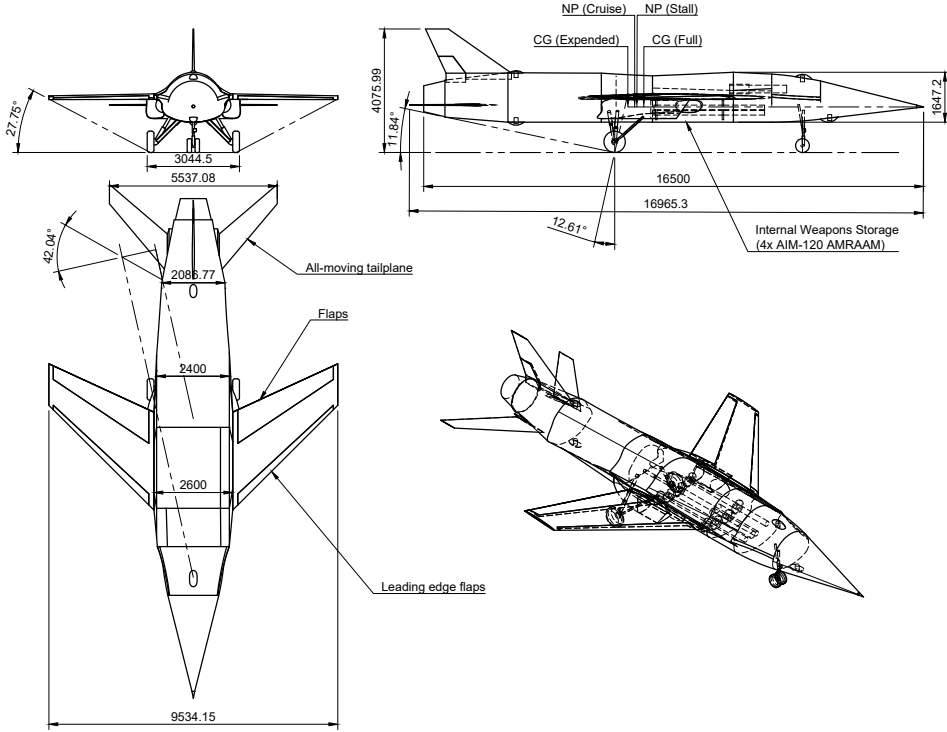


Figure 1: Three-view and perspective drawing of the aircraft

As the aircraft deploys payload, the static margin was shown to shift to negative values. The center of gravity moves backwards, to 9.7613 m aft of the nose tip. The neutral point at landing speed moves a small amount to 9.48 m, placing the static margin at around -9.48%, a region of moderate instability, but within the specified bounds; especially for landing, limit exceedance for static margin may increase the risk of crash. In any case, our static margin values will necessitate the integration of a flight control system. Our aircraft has sufficient internal volume for an additional system, and considering most frontline fighter aircraft currently in service integrate some form of a flight control computer to facilitate enhanced maneuverability, this will not detrimental to our design.

In a holistic survey, the Libellula F-81 is a single-engine, lightweight dedicated supersonic interceptor that not only prioritizes cost, but also aerodynamic and combat efficiency in being able to quickly intercept any threat to the homeland.

### 1.3 Performance Parameters

Table 2: Performance Parameters

Parameter	Libellula F-81	F-35A	F-16	F-22
Takeoff Weight (kg)	13,880	31,750	16,875	38,000
Empty Weight (kg)	7,560	13,300	8,570	19,700
Payload (kg)	1,280	8,165	7,711	9,072
Number of Missiles	4	6	6	6
Cruise, Takeoff, Landing $C_L$	0.58, 1.36, 0.89	0.74, 1.3, 0.9	0.2, 1.45, 0.9	0.35, 1.65, 1.0
Cruise $L/D$	9.485	15	10	8.4
$T/W$ max	1.06	0.87	1.1	1.08
$W/S$ ( $\text{kg}/\text{m}^2$ )	550	742	610	483
Engine type & max SLS thrust	F110-GE-132, 142 kN	F135-PW-100, 191 kN	F100-PW-200*, 89 kN	F119-PW-100, 311 kN
Engine cruise SFC ( $\text{kg}/\text{N/h}$ )	0.067	0.9-1.0	0.78-0.85	0.9
Span (m)	9.534	10.668	9.99744	13.5636
Reference Area ( $\text{m}^2$ )	25.25	42.74	27.87	78.04
Aspect ratio	3.6	2.66	3.59	2.36
Average wing $t/c$	5%	-	-	-
Cruise Mach no. (Max and Economic)	1.6, 0.85	1.6, 0.85	2.0, 0.8	2.25, 0.85
Maximum range (nm)	3.03E+06	1,380	2,280	1,839
Maximum range fuel burn (kg)	10,714	11,000	8,500	12,000
Payload**	4x AIM-120, 1x M61A1	4x AIM-120, 2x AIM-9	2x 2,000 lb bombs, 2x AIM- 9, 2x AIM-120, 2x 2,400 lbs external tanks	2x 1,000 lb GBU- 32, 2x AIM-120, 2x AIM-9
Static margin	0.04	-	-	-
Maximum landing distance (m)	8,000	2,438	900	2,438
Maximum takeoff distance (m)	8,000	2,438	1,100	480
Avg. flyaway cost for 250, 500, & 1000 units (USD)	18.04M, 17.14M, 16.3M	100M, 80M, 70M	30M, 25M, 20M	150M, 120M, 100M

\*Multiple engines available

## 2 Introduction

Due to rising geopolitical tensions, we were tasked with designing a Homeland Defense Interceptor (HDI) aircraft that is agile, cost-effective and dedicated to defending U.S. airspace. Our design seeks to fill a crucial gap left by current Air Force and Navy fighter fleets, which are too expensive to field in sufficient numbers for the intended missions. The goal of this project is to provide an affordable, high-performance solution that ensures sufficient homeland defense coverage without diverting funds from offensive force capabilities.

Our HDI aircraft will support three core mission profiles, each with distinct operational demands. The primary, and most constraining, is the Defensive Counter-Air mission, which requires extensive fuel capacity due to its endurance and range demands, resulting in a higher overall weight necessary for the aircraft. Additionally, the HDI aircraft will complete a point defense intercept mission, focused on high-speed, short duration interceptions, and an intercept and escort mission for protecting other aircraft over a set range. Depictions of each mission profile are provided in Figures 2, 3, and 4. These missions collectively define the operational flexibility necessary to counter diverse airspace threats while maintaining budgetary and logical feasibility.

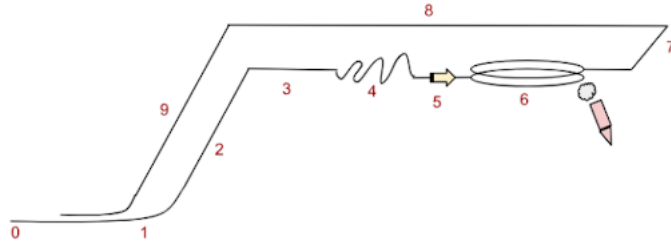


Figure 2: Defensive Counter-Air Patrol Mission Profile

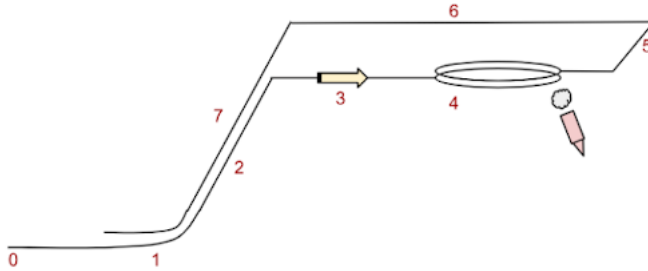


Figure 3: Point Defense Intercept Mission Profile

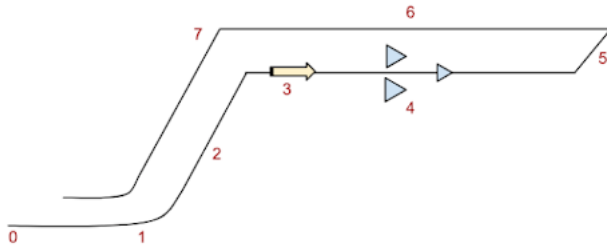


Figure 4: Intercept and Escort Mission Profile

Our design and performance requirements are centered around cost-effectiveness and operational efficiency. The HDI must be remotely piloted, removing the need for an onboard pilot, and allowing for a smaller, streamlined airframe. To ensure we meet the budget constraint of staying below 25 million dollars per aircraft, the design will incorporate practical measures to reduce complexity and streamline maintenance capabilities. The HDI will operate in all weather conditions and from standard NATO runways, making it

adaptable to various environments and ready for rapid deployment by 2027. A further breakdown of the design requirements is provided in Figure 5.

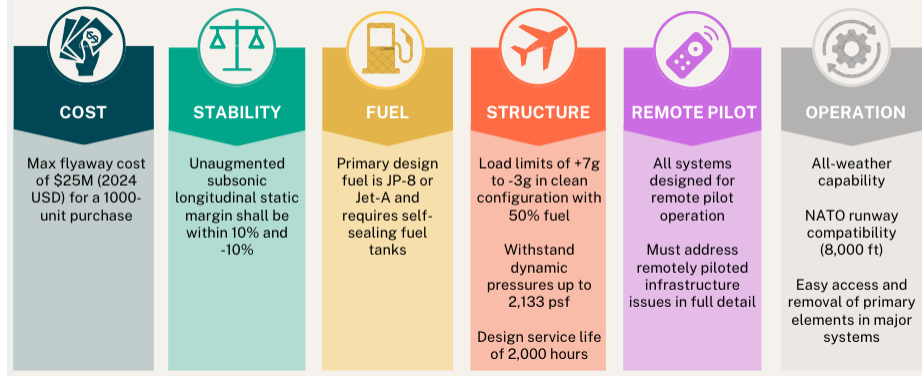


Figure 5: Design Requirements of the Aircraft

Additionally, the HDI is designed to meet rigorous performance standards necessary for effective homeland defense. It must achieve a maximum mach number of 1.6 at an altitude of 35,000 feet, allowing it to intercept and engage high-speed threats swiftly. Specific excess power requirements are set for various altitudes and speeds, ensuring strong acceleration and climb capabilities essential for both immediate threat response and sustained combat maneuvers. The aircraft must sustain a load factor up to 5 G's under maximum thrust conditions, enabling sharp turns and agile responses during high-stakes engagements. Furthermore, the HDI must meet endurance requirements for long-range missions, such as maintaining combat air patrol for hours at a 300 nm radius. A more detailed breakdown of the performance requirements the HDI must meet are provided in Figure 6. These performance capabilities ensure that the HDI can efficiently patrol, intercept, and neutralize a range of airborne threats, enhancing the security of U.S. airspace.

Mission Performance	<ul style="list-style-type: none"> <li>Intercept mission radius of 200 nm</li> <li>DCA combat air patrol endurance of 4 hours at a 300 nm radius from base</li> </ul>
Performance at Maneuver weight (50% internal fuel)	<ul style="list-style-type: none"> <li>Max Speed of M = 1.6 at 35,000 ft</li> <li>Maximum Instantaneous Turn Rate at 35,000 ft is 18.0 deg/s</li> <li>Military Thrust: <ul style="list-style-type: none"> <li>1-g Specific Excess Power - 200 ft/s (SL) and 50 ft/s (15,000 ft)</li> </ul> </li> <li>Maximum Thrust: <ul style="list-style-type: none"> <li>1-g Specific Excess Power - 700 ft/s (SL) and 400 ft/s (15,000 ft)</li> <li>5-g Specific Excess Power - 300 ft/s (SL) and 50 ft/s (15,000 ft)</li> <li>Sustained load factor of 5.0 g's at 15,000 ft</li> </ul> </li> </ul>

Figure 6: Summary of Performance Requirements of the Aircraft

### 3 Considerations for Remote Piloting

The Libellula F-81's design emphasizes advanced technological and infrastructural integration tailored for fully remote operations. Without an onboard pilot, every system must operate autonomously and handle all conceivable scenarios with reliability. Drawing insights from similar high-speed UAVs, such as the Exosonic Revenant, Lockheed D-21, and XQ-58 Valkyrie, we recognized the necessity of robust visual capabilities. This led to the selection of Trillium Engineering HD45 gimbals as the core imaging system, ensuring comprehensive situational awareness in both day and night or low-visibility conditions.

Table 3: Trillium Engineering Gimbals

Parameter	Value
Configuration	HD45-LV-CZ
Weight	1.28 kg
Dimensions (WXH)	0.134 x 0.197 m
Resolution	Visible: 1280 X 720 LWIR: 640 X 512
FOV	Visible: 13.7-4.6 [deg] LWIR: 29-5.9 [deg]
Zoom	8-10X
Price / Unit	55K

The HD45 gimbals offer electro-optical and infrared imaging, which are critical for the Libellula F-81's operations across varying visibility scenarios. Their compact, low-SWaP-C (size, weight, and power-cost) design aligns with our performance requirements, enabling minimal power consumption and maximum efficiency. Additionally, this model has a TRL of 9 for military applications, providing further confirmation that this system will be suitable for use in the intended missions. With onboard capabilities such as real-time attitude, velocity, and position data through co-located IMUs and geo-tracking, these gimbals provide essential system redundancy. For military UAVs, redundancy is vital—backup systems ensure operational continuity even if primary avionics are compromised by hostile engagements or mechanical failure. The gimbals' continuous 360° pan and adjustable tilt range (-80° to +42°) complement the aircraft's strategic placement of cameras at 10-degree angles. This configuration eliminates overlapping blind spots directly above and below the aircraft, enhancing situational awareness without compromising field of view. As can be seen in 8, the individual blind spots of each camera can be observed as a blue conic region emitted by the aircraft. It is important to note that with the placement of 4 external gimbals, as can be seen in the diagram, each camera's individual blind spot is accounted for by the other camera present on the same surface. More specifically, the blind spot created from the upper surface, aft-most camera is completely visible from the upper surface, front-most camera.

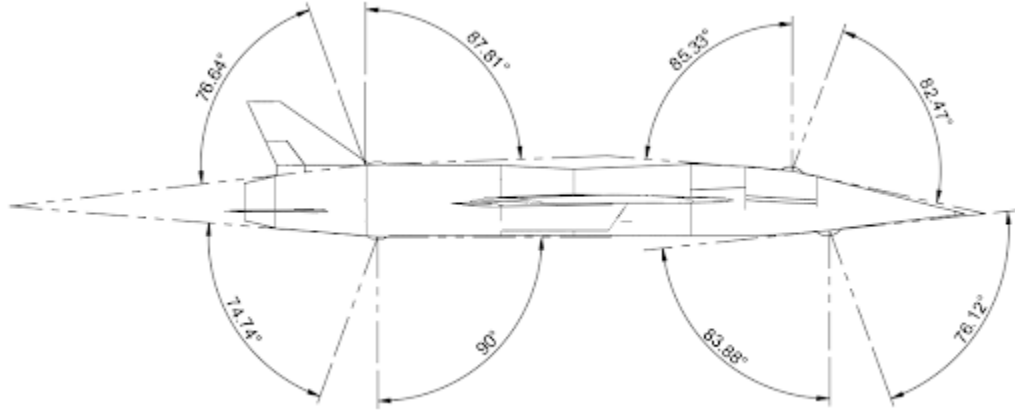


Figure 7: Camera clearance angles with the fuselage

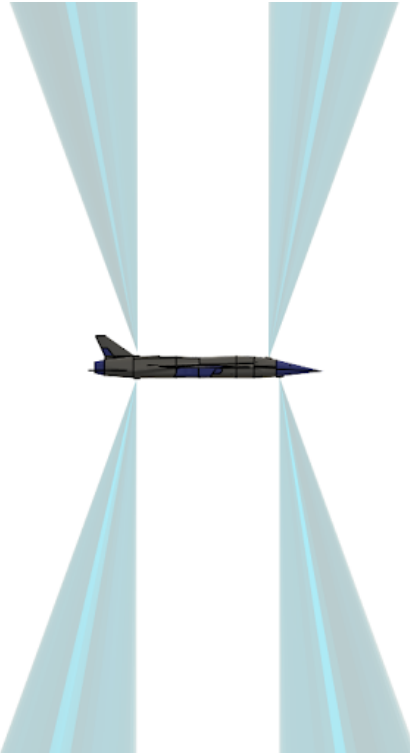


Figure 8: Blind spots of each individual camera on board

Latency and bandwidth are also common challenges in remote UAV operations, especially during high-speed maneuvers or missions that require real-time decision making. To address these, the Libellula F-81 employs HD45 gimbals equipped with h.264-compliant onboard video compression and adjustable bitrates, optimizing data streams to ensure minimal latency. In addition, our systems leverage a dedicated military-grade communication infrastructure that balances high data rates and robust encryption. This secure pipeline minimizes the risk of interference or breaches, ensuring seamless control and data transmission under extreme operational conditions.

Finally, secure communication is paramount in military UAV operations. The Libellula F-81 plans to use military-verified private channels, avoiding the vulnerabilities of public networks. These channels are protected against cyber threats through proprietary encryption protocols and transmission methods. This approach protects mission-critical data and enhances command-and-control reliability, ensuring that the F-81 remains a trusted asset in the most sensitive military scenarios. Combined, these innovations underscore the Libellula F-81’s readiness for autonomous operations in the most demanding environments.

## 4 Configuration

In designing the Homeland Defense Interceptor aircraft, the primary objective is to minimize costs while creating a compact, straightforward design that meets mission requirements for maneuverability, endurance, and armament capacity. To achieve this, we have prioritized a minimalistic design philosophy, ensuring the aircraft is as small and lightweight as possible while maintaining sufficient storage for essential weapons, equipment, and fuel. The design has matured significantly since the preliminary design, and will be discussed in more detail in the following sections. Given the high maneuverability demands in our Defensive Counter-Air Patrol and Point-Defense Interception missions, our configuration is designed to be moderately unstable for later phases of flight. This slight instability enhances agility, as seen in many advanced fighter designs, which utilize controlled instability to meet high maneuverability requirements. Further analysis of stability and control specifics has been covered in II.B which covers the 3-D design of the aircraft.

Our interior storage is engineered to carry four AIM-120 missiles internally. Although initial storage was of six missiles, it was deemed that six was too excessive especially considering we pursued an internal weapons bay as the added cost of two more missiles; additionally, for a mass-produced low-cost interceptor design such as this, the added benefits of two additional missiles are marginal at best. Furthermore, without the need for a pilot or cockpit, as this aircraft will be remotely piloted, we were able to optimize fuselage space for additional fuel and mission-critical equipment. This layout contributes to the efficiency and simplicity of the design by eliminating traditional cockpit infrastructure, allowing more compact and modular systems.

Configuration decisions for the wing, empennage, and fuselage are detailed in Sections VIII. Aerodynamics, and VI. Interior Layout, respectively. In line with our design objectives, all major systems have been integrated to allow easy access and removal, facilitating operational maintenance and repair requirements. This modular, straightforward approach not only reduces costs but also supports faster deployment and turnaround times for essential equipment replacement. An overall isometric view from the top and bottom of the aircraft is shown in figure 9, showcasing the features of the aircraft, prominently the internal weapons bay as seen from the bottom with doors removed, revealing the missile load; note that the missiles are cylinders only intended to model the general geometry of the AIM-120.

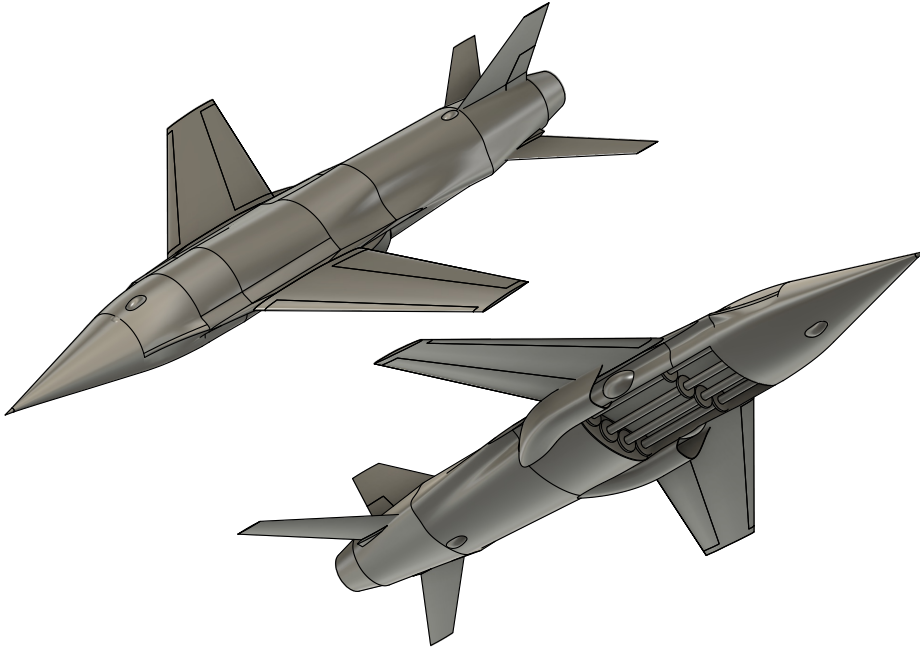


Figure 9: Aircraft configuration showcase

## 5 Preliminary Sizing

This section outline the key steps in our approach to aircraft sizing, beginning with an initial weight estimate that considers mission fuel requirements, payload, and equipment, forming a foundation for further design refinements. Next, we present  $T/W$  vs.  $W/S$  plots to examine how thrust-to-weight and wing loading choices satisfy our mission and regulatory constraints, an improved weight estimate, and finally, we analyze a  $T$  vs.  $S$  plot, where cost objective function contours are overlaid to visualize the trade-offs in thrust and wing area for cost-effectiveness and mission performance. For more details on the computational methods and software implementation used to generate these plots, please refer to the Computational Procedure and Software Design section (16).

## 5.1 Initial Weight Estimate

Our initial weight estimation process was a key step in the preliminary sizing of the aircraft, allowing us to align potential design considerations with mission requirements and constraints. To begin, we broke down the mission profiles and analyzed each segment to estimate engine fuel consumption. Using historical data on fuel fraction estimates from Raymer [1], we calculated fuel needs for each mission segment, which revealed that the Defensive Counter-Air (DCA) mission required the most fuel, making it the primary driver in our weight estimation approach. Applying variations of the Breguet range equation along with historical fuel fraction values, we estimated fuel consumption for each segment relative to the previous one, creating a comprehensive profile of fuel requirements across all mission phases. These fuel estimates were then correlated with takeoff gross weight (TOGW) using historical data, providing a well-grounded basis for our initial weight figures.

Our design choice to operate the aircraft remotely allowed us to exclude weights associated with crew and life-support systems, focusing instead on camera and remote pilot equipment. Additionally, the weight of the four AIM-120 missiles and a fully loaded M61A1 cannon was factored into the payload, based on weights specified in the Request for Proposal (RFP). Together, these considerations helped us refine our weight estimate, ensuring the design was well-aligned with the operational requirements while keeping the overall weight as low as possible.

## 5.2 T/W vs W/S

Our approach to generating the  $T/W$  vs.  $W/S$  plots was essential for selecting an optimal design point that met mission and operational constraints. First, we represented the operational requirements and mission phases as constraints, including takeoff and landing distances, flight ceiling, stall speed, maneuverability, climb capability, and excess power requirements.

For takeoff and landing, we used NATO's runway length standard of 8,000 ft, with equations 22, and 21 to calculate these constraints accurately. Climb requirements were based on meeting regulatory climb gradients, ensuring adequate operational performance in different mission phases. Maneuverability constraints were differentiated between instantaneous and sustained turns as specified in the RFP. For sustained turns, we selected a roll angle of 60 degrees (equivalent to a 2g load) which is typical for fighter jets [2]. The instantaneous turn was calculated from equations 23, 24, and 25, and the sustained turn was calculated from equations 26, 27, and 28. The rest of the constraint equations are highlighted in part D of the appendix.

By plotting all of these constraints together, we determined feasible regions within the  $T/W$  vs.  $W/S$  space, which guided our selection of a preliminary design point that was capable of meeting all requirements. The feasible region for max thrust is to the left of the landing field length constraint and above specific excess power at 1g, SL. For military thrust, it is to the left of the landing field length constraint, above specific excess power at 1g, SL, and above our takeoff climb.

From this  $T/W - W/S$  diagram, we selected a design point manually by observation, selecting the point with lowest  $T/W$  and highest  $W/S$  value within the feasible region. These plots and the selected design points are shown in Figures 10, 11 and Table 4. An alternate figure with all constraints plotted together is shown in Figure 50 in the appendix.

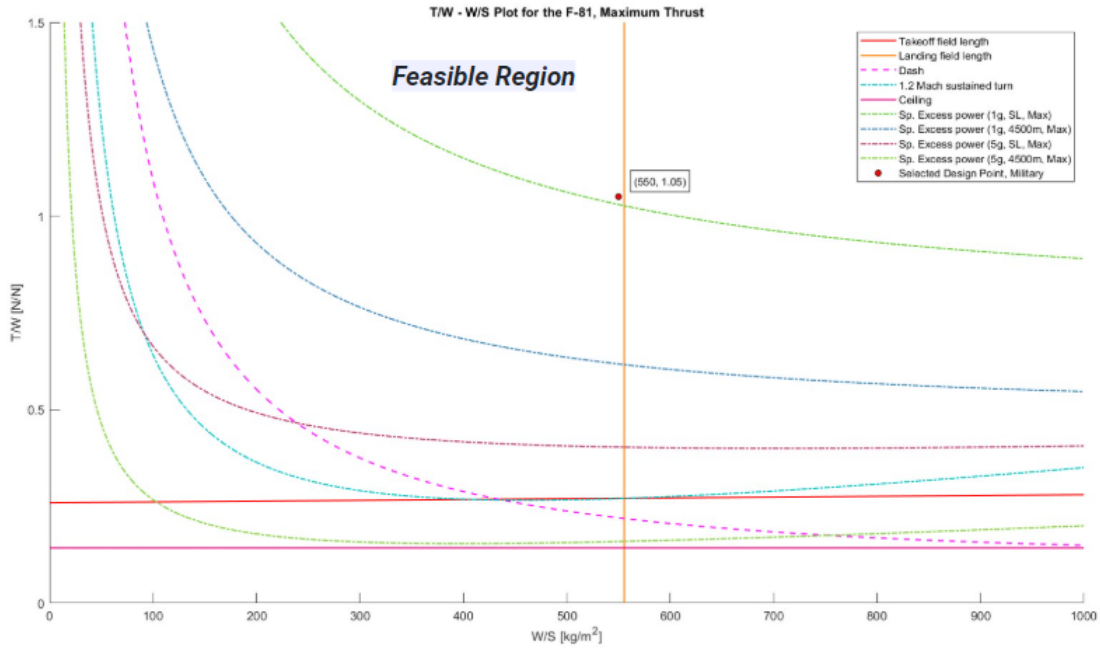


Figure 10:  $T/W - W/S$  Plot, Max Thrust

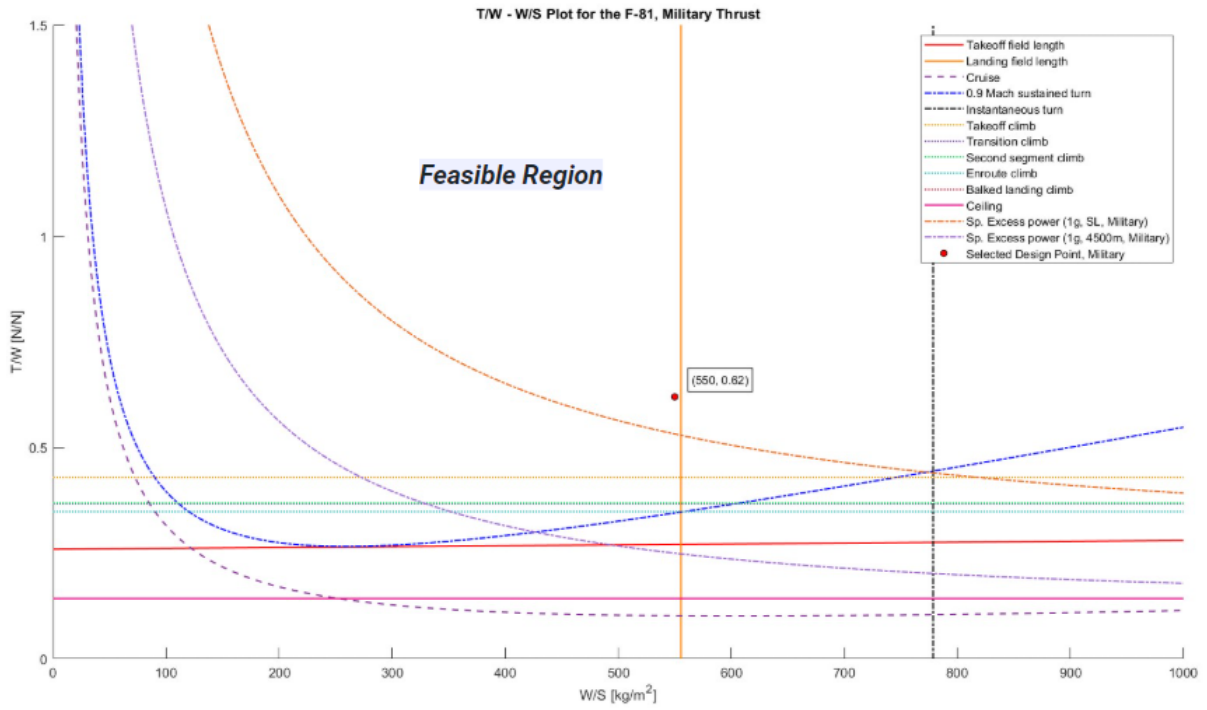


Figure 11:  $T/W - W/S$  Plot, Military Thrust

Our selected design points are indicated on the graph, and repeated again in Table 4 for clarity:

Table 4: Selected Design Points

Parameter	Value
Wing Loading ( $W/S$ )	550 kg/m <sup>2</sup>
Maximum Thrust-to-Weight Ratio ( $T/W$ ) <sub>max</sub>	1.05
Military Thrust-to-Weight Ratio ( $T/W$ ) <sub>military</sub>	0.62

### 5.3 Improved Weight Estimate

Our updated weight calculations provided a more accurate takeoff gross weight (TOGW) estimate by incorporating refined parameters based on the design points selected from our T/W vs. W/S plots. This updated process calculates empty weight using a regression model, where the design wing area and design thrust values are derived from TOGW and the selected design ratios. Adjustments to the empty weight account for specific input values of thrust ( $T$ ) and wing area ( $S$ ), applying area density adjustments and engine weight regressions from  $T$  to refine accuracy. With these updated empty weight values, we estimate a new fuel fraction based on wetted surface area and drag characteristics, incorporating them into the Breguet Range equation. The TOGW is iteratively refined through these steps until convergence is achieved, resulting in a more accurate weight estimate for the final design. Because this function also depends on  $T$  and  $S$ , we were able to plot cost contours (our objective function, discussed in section 10, which depends on TOGW) over our  $T - S$  diagram in order to select a point at minimum cost.

### 5.4 $T$ vs $S$ with objective function

Using the selected  $T/W$  and  $W/S$  design point along with our updated TOGW estimate function, we were able to plot the same constraints in the space of  $T$  and  $S$ , enabling us to select these key parameters for our aircraft design. Details on the computation of  $T$  and  $S$  from these inputs is discussed in section 16.

The space to the right of the landing field length line and above specific excess power at 1G, SL, for maximum thrust dictates our feasible region for  $T$  max and  $S$ . The space to the right of the landing field length line and above specific excess power at 1G, SL, for military thrust dictates our feasible region for  $T$  military and  $S$ .

By overlaying TOGW contours over these constraints, we reached our final  $T$ - $S$  plot as shown in figure 12 and selected  $T$  max,  $T$  military, and  $S$  for our design. Cost was very sensitive with respect to  $T$ , and less so with  $S$  - confirming the dominant proportionality of thrust and aircraft cost. Identifying a point that minimized cost and gave some margin (which provides some flexibility if/when TOGW estimates increase), we selected  $25.25m^2$ ,  $84.5kN$ , and  $144.6kN$  for wing area, military, and maximum thrust, respectively. The yellow and orange dashed lines represent maximum and military thrust values, respectively for our selected engine (discussed in section 11). An alternate figure with all of our  $T - S$  constraints as shown in figure 51.

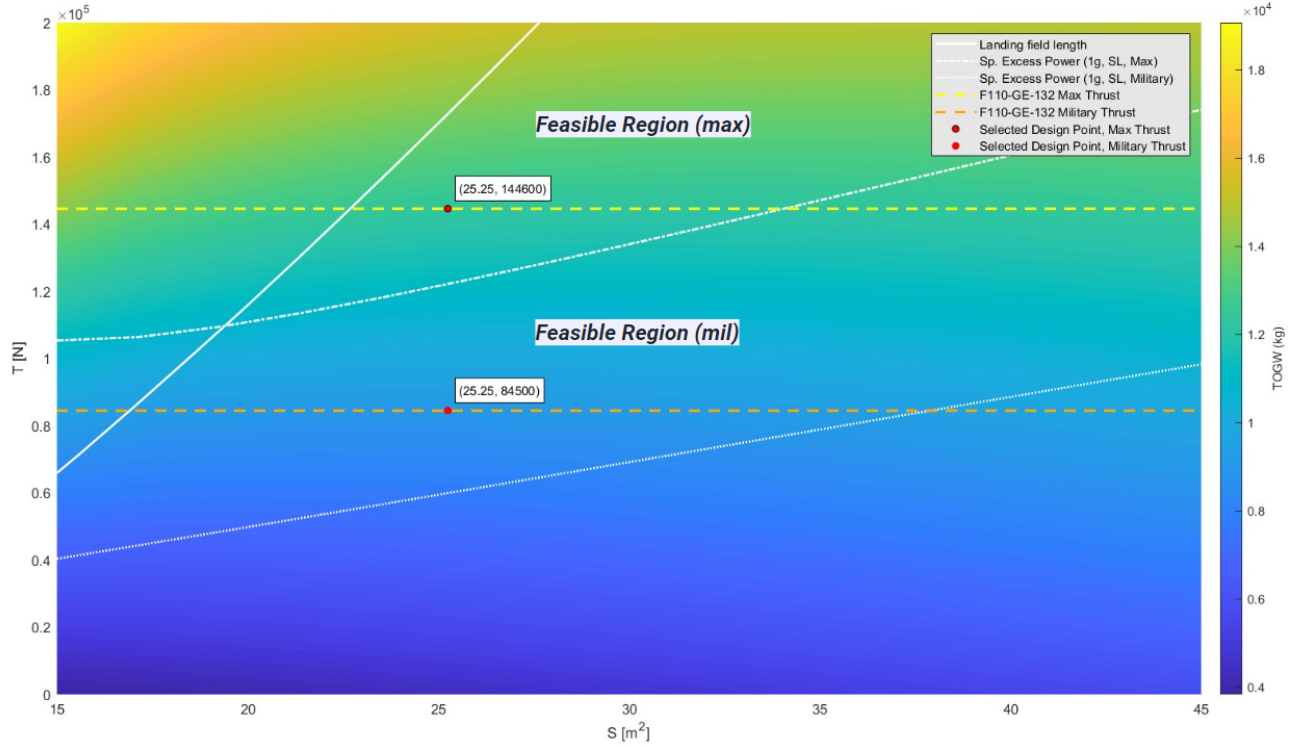


Figure 12:  $T - S$  Plot, constraining lines plotted over TOGW

To summarize, the final aircraft parameters decided from the  $T - S$  plot are listed in Table 5. The TOGW, empty weight, and DCA fuel fraction calculated from our updated functions for these selected  $T$  and  $S$  values are listed in Table 6.

Table 5: Selected Aircraft Parameters

Parameter	Value
Maximum Thrust ( $T_{\max}$ )	144,600 N
Military Thrust ( $T_{\text{mil}}$ )	84,500 N
Wing Area ( $S$ )	25.25 $m^2$

Table 6: Updated Aircraft Weight Parameters

Parameter	Value
Fuel Fraction (DCA Mission)	0.385
Empty Weight ( $W_e$ )	7,560 kg
Takeoff Gross Weight ( $W_0$ )	13,900 kg

## 6 Interior Layout

### 6.1 Fuselage

The fuselage features a dual under-wing diverterless engine inlet. This leverages fuselage internal volume allocation and simplicity in design, as this configuration eliminates the need for complex variable geometry for the inlets, but simultaneously requires a larger total fuselage width to accommodate enough capture area for the engine. Especially for our engine choice, which features a larger bypass ratio than the typical military turbofan engine, each inlet required a relatively large cross-sectional area to ensure enough airflow is provided for the engine. Even so, this, at least partially, isolates the inlet section and the main body of the fuselage, allocating much more internal volume for fuel or payload.

Additionally, the fuselage was subjected to more area ruling. With the absence of the top-mounted inlet, and the reduction of fuel volume, it was found that the cross-sectional area of the fuselage could be further reduced. To better facilitate area ruling, the wings were integrated with the fuselage with a blended-wing design, accomplished with strategic lofting of fuselage sections with the wing root. The resulting final design features a local minimum in the fuselage height halfway down the length of the fuselage, along with a seamless connection between the fuselage and the wings, complete with leading edge extensions.

### 6.2 Interior Components

The configuration of interior components were modified to some degree, but was not significantly different from the preliminary design. Figures 13 and 14 show isometric views of the aircraft interior, highlighting the different component families by color. Notably, the fuel tanks, highlighted in yellow, take up the most internal volume. To alleviate concerns for excessive movement of the center of gravity, the tanks were installed such that the distribution is roughly even. The avionics equipment, highlighted in dark blue, includes all tracking, communication and aircraft control components. The propulsion system, highlighted in green, includes the engine, its APU, and the associated electrical systems. The weapons, highlighted in red, includes the 4 AIM-120 missiles and the M61A1 cannon and feed system. Finally, the landing gear, highlighted in gray, includes the main and nose gear assemblies. A gap exists in front of the engine face and the landing gear housing to accommodate the diffuser ahead of the engine inlet.

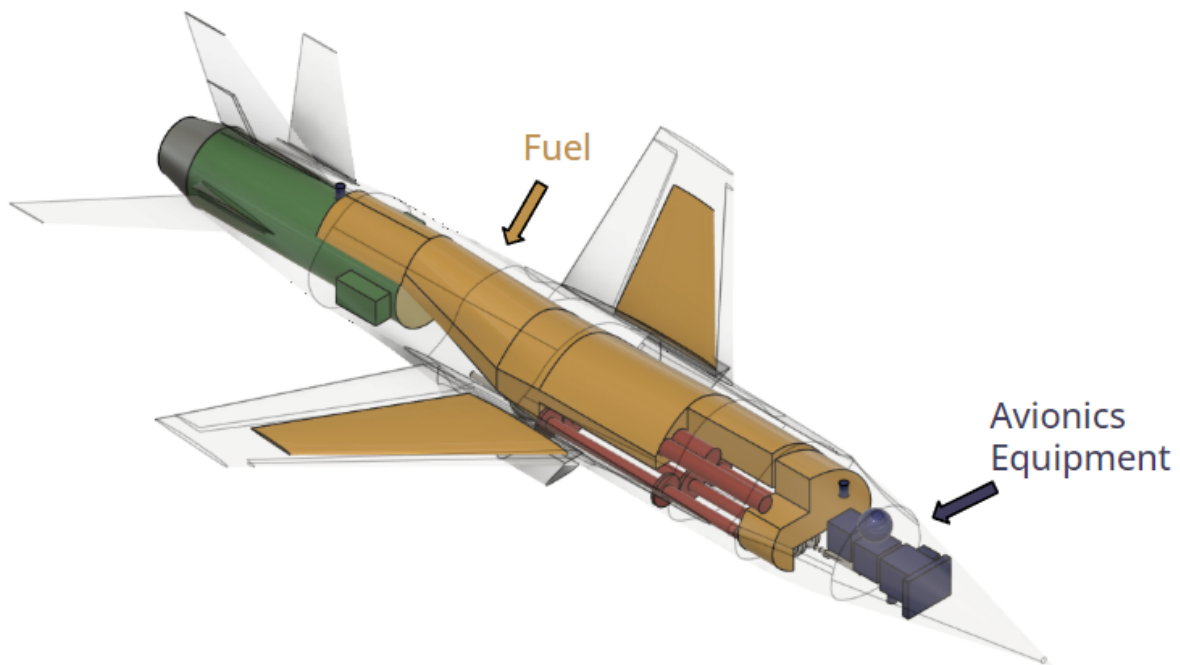


Figure 13: Aircraft interior diagram - top isometric view

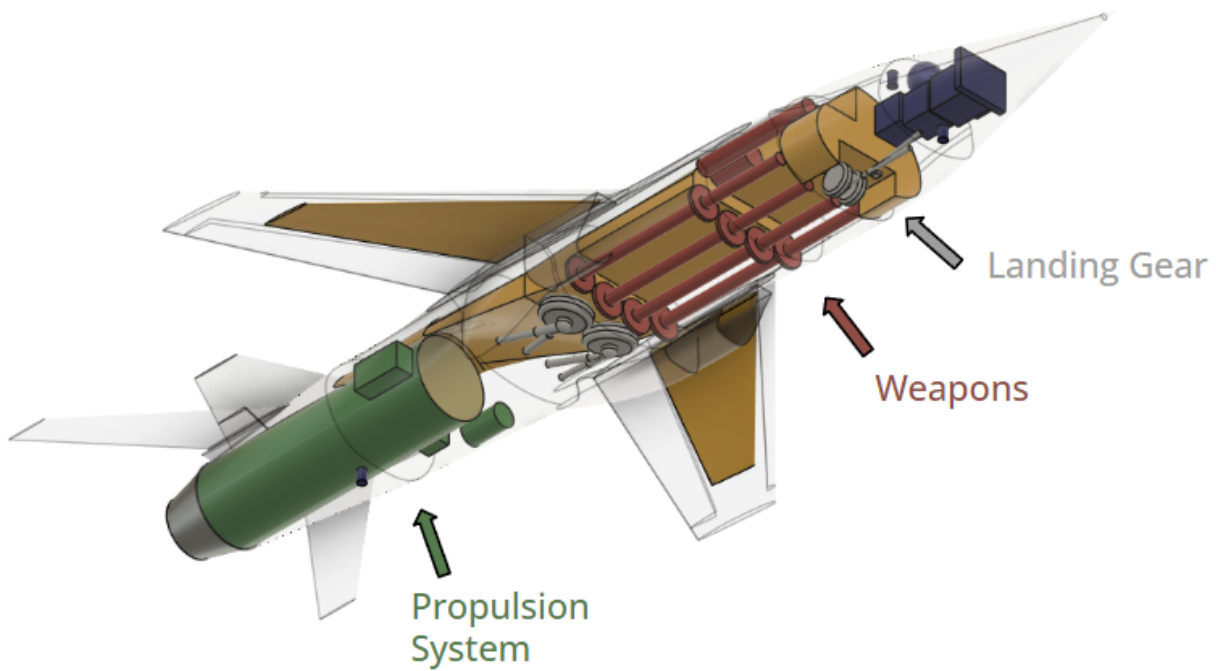


Figure 14: Aircraft interior diagram - bottom isometric view

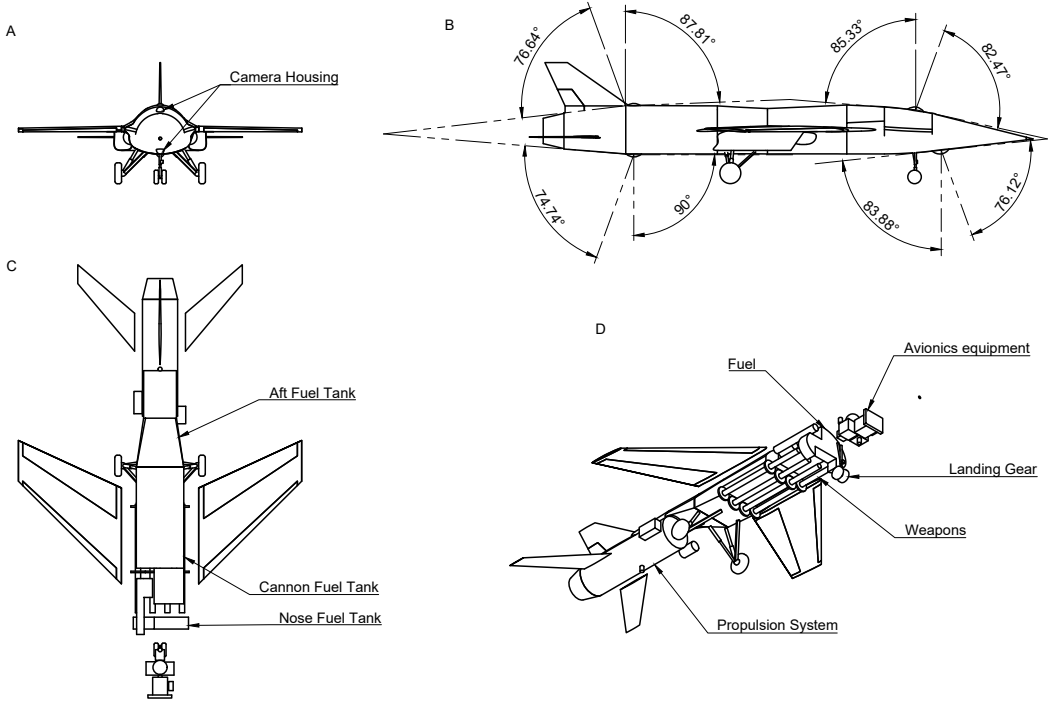


Figure 15: Aircraft interior breakdown with camera angles, fuel tanks, and payload

View B in figure 15 outlines the fields of view for each of our four cameras located around the aircraft. As discussed in the remote piloting considerations section, the front cameras were installed at a 10 degree angle forward, and the rear cameras at 10 degrees backward, to ensure the blind spots of one camera can be covered by another. View C showcases the naming schemes for the fuselage internal fuel tanks. The missiles are stowed in an internal weapons bay, exposed in view D, large enough to house four AIM-120s. The smaller volume of the internal weapons bay allowed the enlargement of the cannon fuel tank, which restricted the movement of the center of gravity to some degree as the fuel tank is located relatively closer to the center of gravity. The center of gravity excursion as fuel and payload is depleted is described in the next section. The cannon sits atop the weapons bay, along with its drum magazine, and fires out of a cannon port located to the right side near the termination of the nose cone.

## 7 Component Weight Breakdown

To more accurately predict the weight of our aircraft, we produced a more granular estimate by calculating the expected weight of each component, including airframe components, landing gear, fuel, payload, and avionics. Table 7 indicates the method used to calculate the weight of each component, the source of this method, and the weight.

Surface areas for the above calculations involving  $S_{wet}$  were pulled from our CAD model. Additionally, ‘fudge factors’ were applied to various components to account for lighter manufacturing methods that have emerged since these regressions were made. These fudge factors were pulled from Raymer [1] Table 7.5. We used the lowest value in the ranges presented in the table, as we assume we are using the best manufacturing technologies on the market (and have accounted for this in the cost calculation 10): 0.85 for the wing, 0.83

Component	Weight Calculation Method	Source	Weight [kg]
Payload	Sum of included missiles, cannon, and ammunition	RFP	985
Fuel	Segmented fuel fraction buildup	Lecture 13 - Refined Sizing [3]	5340
Fuselage	23 kg/m <sup>3</sup> of wetted area	Raymer Table 15.2 [1]	1960
HTail	20 kg/m <sup>3</sup> of wetted area	Raymer Table 15.2 [1]	58.0
VTail	26 kg/m <sup>3</sup> of wetted area	Raymer Table 15.2 [1]	45.7
Engine Dry Weight	Sourced online	GE F110 Wikipedia [4]	1840
Engine Wet Weight	Engine mass regression from selected engine thrust	Metabook 7.14 to 7.18 [5]	1840
LG	3.3% of TOGW	Raymer Table 15.2 [1]	458
Extra	14% of TOGW	Reduced from the 0.17 in Raymer Table 15.2 [1], as modern avionics are lighter	1420
Wing	Regression for Airforce fighter jet wings	Roskam Part 5, Eq. 5.9 [6]	1200
<b>Total</b>			<b>13900</b>

Table 7: Component Weights

for the tail, and 0.9 for the fuselage.

These component values were iteratively calculated and summed until a final TOGW was converged upon, which serves as our final TOGW estimation at this stage in design: **13,900 kg**. This value was 11.2% higher than our initial estimate, which calculated TOGW as a function of T and S alone. This necessitated a new engine selection and resizing to ensure we stayed within our feasible space given by our constraint diagram 50.

Figure 16 visualizes the breakdown of payload, fuel, and empty weight. Figure 17 visualizes the breakdown of components that make up the empty weight of the F-81.

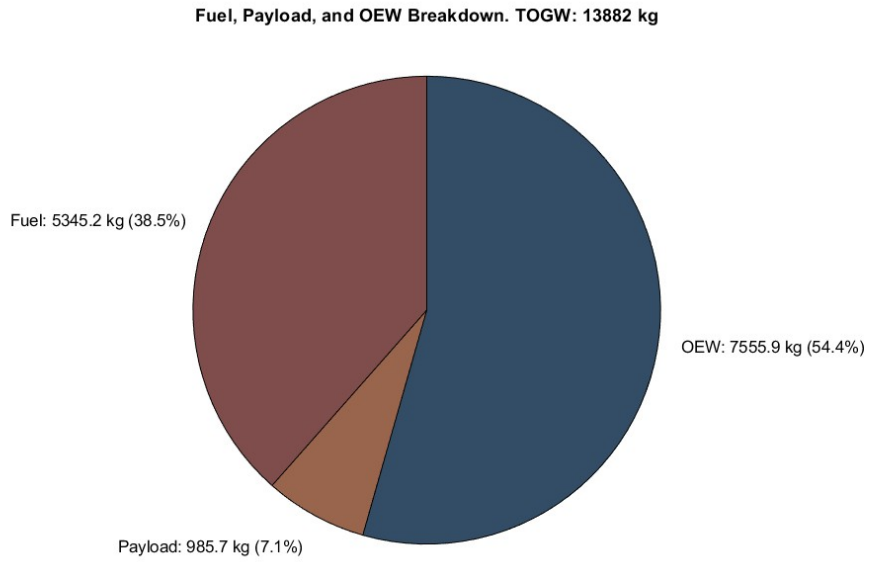


Figure 16: Weight Breakdown of Aircraft

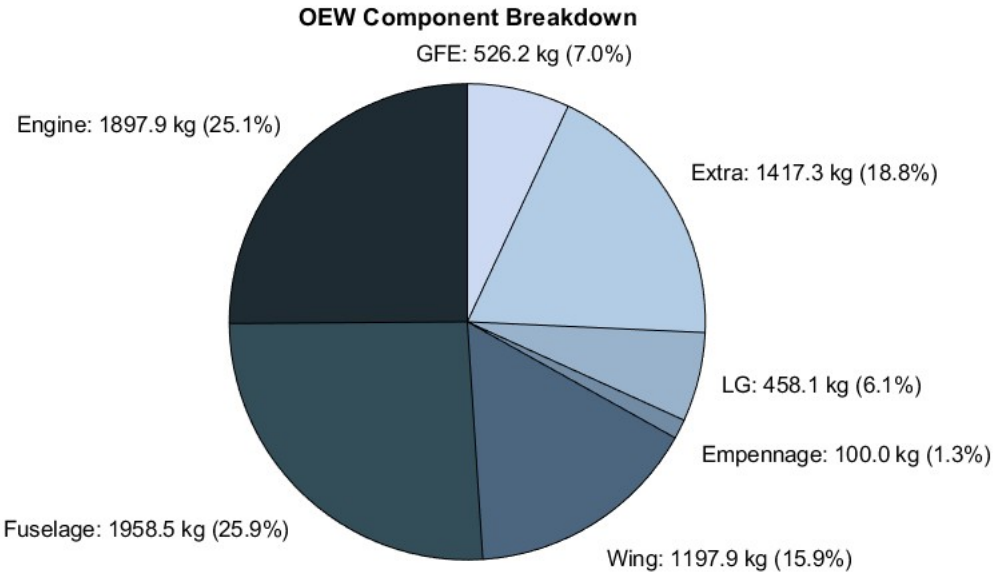


Figure 17: Weight Breakdown of Empty Weight

## 7.1 Center of Gravity and Aircraft Balance

Using the allocated positions of the internal components of the aircraft as described above, the weight values of Government Furnished Equipment (GFE) from the RFP, considering fuel densities and volumes

in each tank, and using historical values for the CGs of aircraft components (Raymer [1] Table 15.2), the component-wise aircraft weight breakdown was mapped to each component's relative position in the aircraft. This allowed for a more refined analysis of aircraft balance.

The center of gravity was calculated using code that accepts the center of gravity locations and corresponding weights of each component of the aircraft and outputs the overall center of gravity of the complete aircraft. In particular, two states were of interest: the fully loaded state, which includes full fuel and weapons load, and the fully expended payload state, which removes missile and consumed fuel load from consideration. However, to better understand the progression of the movement of the center of gravity, the refueling and rearming process as well as the launching of each missile during flight was considered as separate "states" for consideration. Figure 18 shows the result of analysis of the movement of the center of gravity as a flight progresses.

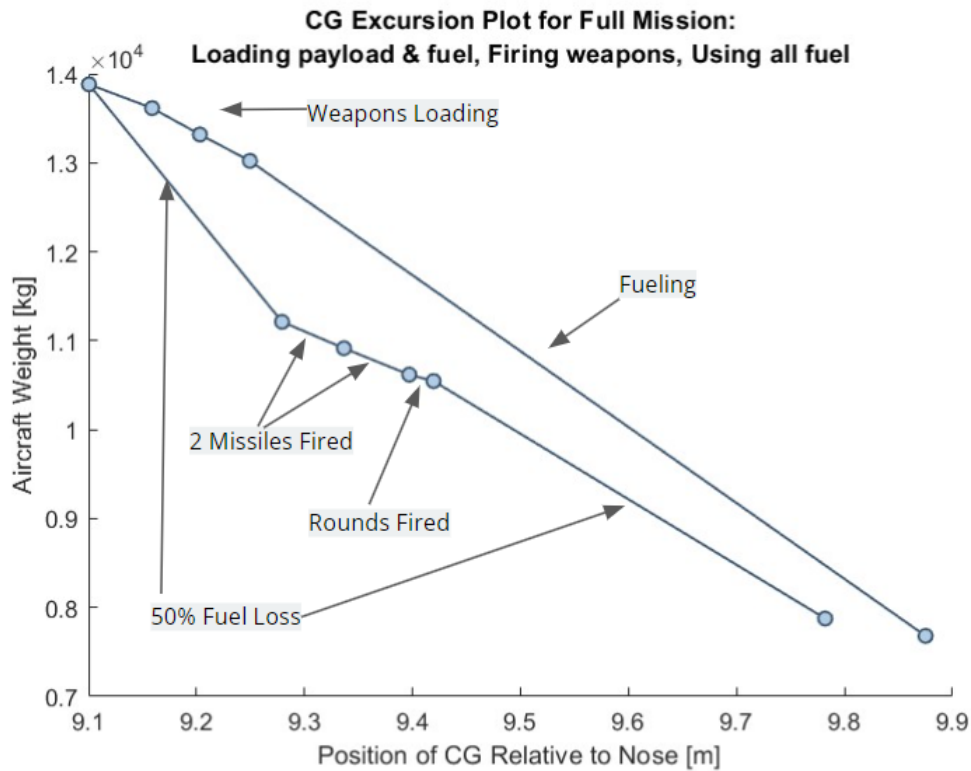


Figure 18: CG Excursion Plot for A Full Mission, Loading to Landing

Figure 18 indicates that the center of gravity begins at 9.8547 m aft of the tip of the nose unfueled and unarmed, and moves continuously forward during the loading process to a final fully loaded center of gravity of 9.2362 m. This poses no threat to aircraft tip-over on the ground as the main landing gear is projected to be located 10.196 m aft of the nose as seen in Figure 1, well behind the rearmost center of gravity. The effects of these changes in C.G. during flight will be discussed in the Stability and Control section.

## 8 Stability and Control

With a highly refined center of gravity estimation, stability analysis was made possible. A fundamental parameter in assessing the stability of the aircraft is the mean aerodynamic chord, which will be referred

hereon as MAC. This is defined as in Equation 1:

$$\bar{c} = \frac{1}{S} \int_{-\frac{b}{2}}^{\frac{b}{2}} c(y)^2 dy \quad (1)$$

The wing design, discussed in 9.1, yields a expression of the wing chord length as a linear function of the spanwise location. Evaluating the integral yields the chord length  $\bar{c}$ , and, using the inverse of the chord formula, the spanwise location  $\bar{Y}$  taken from the root of the wing. They are calculated as follows:

$$\begin{aligned}\bar{c} &= 2.853m \\ \bar{Y} &= 2.001m\end{aligned}$$

The MAC is crucial in determining the static margin of the aircraft and thus the neutral point; these parameters were derived from additional geometric parameters based on the CAD model. An approximation of the static margin, as outlined in *The Metabook of Aircraft Design*[5], is defined as follows:

$$-SM = \frac{x_{CG} - x_{np}}{\bar{c}} \approx \frac{x_{CG} - x_{25\%MAC}}{\bar{c}} + \frac{l_h S_h C_{L_{\alpha h}}}{\bar{c} S_w C_{L_{\alpha w}}} - \frac{\partial C_{m_{fus}}}{\partial C_L} \quad (2)$$

All parameters are immediately available from our integrated 3D model, except select variables;  $C_{L_{\alpha w}}$ ,  $C_{L_{\alpha h}}$  can be approximated with equations from the United States Air Force DATCOM [7] which are defined as:

$$C_{L_{\alpha w}} \approx \frac{2\pi A R_w}{2 + \sqrt{(A R_w / \eta)^2 (1 + \tan^2 \Lambda_h - M^2) + 4}} \quad (3)$$

$$C_{L_{\alpha h}} \approx \frac{2\pi A R_h}{2 + \sqrt{(A R_h / \eta)^2 (1 + \tan^2 \Lambda_h - M^2) + 4}} \left(1 - \frac{2C_{L_{\alpha w}}}{\pi A R_w}\right) \eta_h \quad (4)$$

Where  $C_{L_{\alpha h}}$  takes into account the downwash on the tail from the wake of the main wings. For these equations,  $\eta$  and  $\eta_h$  were taken to be 0.97 and 0.8 respectively, the latter being based on the evaluation that a tail higher than the main wing will be less efficient than a lower tail since it will be affected more by the wake in positive angles of attack. Additionally,  $\frac{\partial C_{m_{fus}}}{\partial C_L}$  was estimated based on an empirical formula developed by Robert R. Gilruth [8]:

$$\frac{\partial C_{m_{fus}}}{\partial C_L} \approx \frac{K_f w_f^2 L_w}{S_w \bar{c} C_{L_{\alpha w}}} \quad (5)$$

Where  $K_f$  describes an empirically derived coefficient relating the wing quarter chord position and its effect on the fuselage contribution on the static margin. This was estimated to be 0.718 for our aircraft. All other parameters are either known or derivable from the model, and two cases were considered for  $M$ : A cruise condition, and a takeoff/near stall condition, for which Mach numbers of 0.85 and 0.28 were used respectively; both were evaluated using a fully-loaded aircraft center of gravity. The resulting static margins and derived neutral points were calculated to be:

$$\begin{aligned}SM_{cruise} &\approx 0.1363, x_{np_{cruise}} \approx 9.553m \\ SM_{stall} &\approx 0.1109, x_{np_{stall}} \approx 9.48m\end{aligned}$$

Where the neutral points are stated relative to the tip of the nose. This is a moderately stable aircraft, which is favorable especially during takeoff where static stability is crucial in ensuring a successful takeoff. As such, even if the static margin reaches beyond the  $-10\%$  threshold at takeoff, given the decreasing trend after takeoff, and the fact that all subsequent stages of flight—from cruise to interception to landing—are within the specified bounds, this was deemed to be acceptable; it would be much more favorable to be statically stable during takeoff rather than statically unstable during landing, which could be detrimental for inexperienced pilots.

Considering the movement of the center of gravity as the mission progresses—which was described in the previous section—further calculations were made at differing stages of flight, as well as at different Mach numbers; it is shown in Figure 19 below that the static margin continuously decreases as the flight progresses,

and eventually crosses into a region of moderate instability for all Mach numbers; the absolute minimum was observed in the case of a fully-expended aircraft at Mach 1.6, where  $SM = -0.1175$ . However, this is again considering an configuration representative of landing conditions, not dash; speeds lower than Mach 1.6 will safely fall within the specified static margin bounds, but still will require a flight control system to effectively control the aircraft in the later stages of flight and landing. Figure 20 additionally provides information of how the neutral point changes as the flight Mach changes; it can be observed that the neutral point continuously shifts backwards until  $M = 1.0$ , beyond which the point travels forward again. This corresponds to an initial increase in SM for subsonic speeds then a decrease beyond Mach 1. Refer to Figures 1 for geometric locations of relevant points along the length of the aircraft for the cruise conditions at full and fully expended states. A detailed design overview of control surfaces and empennage components is discussed in a later section.

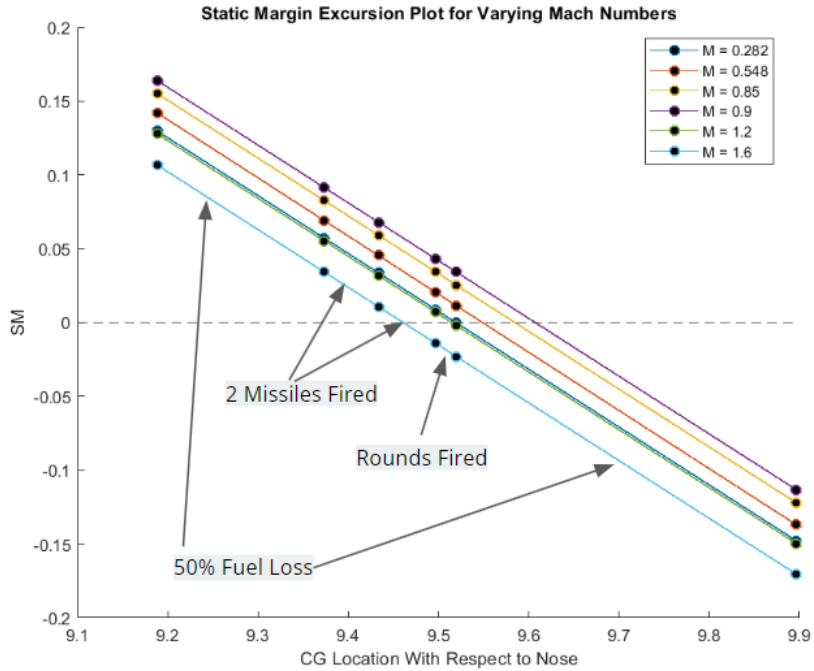


Figure 19: Static Margin excursion plot from takeoff to landing, at differing flight conditions

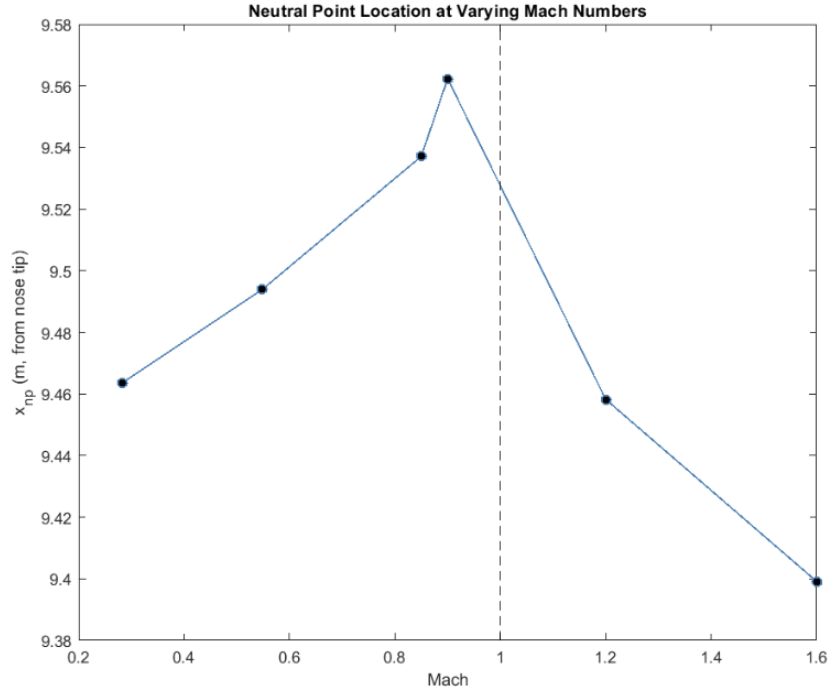


Figure 20: Neutral Point excursion plot with mach number

## 9 Aerodynamics

### 9.1 Wing Design

This section discusses various assumptions and decisions related to the sizing of the wing of the aircraft. Our wing design balances maneuverability, efficiency, and structural integrity of our aircraft in order to meet the requirements of a Homeland Defense Interceptor.

#### 9.1.1 Wing Area

Our wing area increased from  $24.5 \text{ m}^2$  to  $25.25 \text{ m}^2$  after iterative sizing and trade studies provided us a new T-S plot (Figure 12). As mentioned in section 5, a heavier engine was required to meet our updated thrust-to-weight constraint. We were able to minimize the increase in our surface area and therefore avoid adding more weight by finding a combination between wing area and aspect ratio that met our constraints. Given a wing loading of  $550 \text{ kg/m}^2$ , the selected wing area supports the required lift across operation flight ranges for each mission.

#### 9.1.2 Aspect Ratio

An aspect ratio of 3.6 was chosen after observing trends in similar supersonic interceptors such as the F-16 Fighting Falcon [9] and the Lockheed F-104 Star-fighter [10]. We further investigated the advantages of a higher aspect ratio in order to reduce drag at low supersonic speeds and help delay the onset of shocks. Although increasing the AR would increase our maximum L/D, we did not want to make too substantial of a change that could dramatically decrease our stall angle of attack. Ultimately, we choose an AR that minimizes drag by delaying shock formations while preserving lift at higher angles of attack and ensures efficiency at Mach 1.6 with minimal impact on the stall angle and wing area.

### 9.1.3 Span

The wing span was later derived from these two parameters using the following relation.

$$b = \sqrt{AR \times Sref} = 9.534m \quad (6)$$

### 9.1.4 Taper Ratio

Taper Ratio is defined as the ratio of tip chord to the root chord. For supersonic interceptors, using a moderately lower taper can result in reduced wing weight which is beneficial for our high speed segments. We chose a taper of 0.35 because this particular ratio improves our span-wise lift distribution and reduces the induce drag associated with high speeds. Also compared to similar supersonic aircraft, the taper ratio should range between 0.30 - 0.40 for a balance of high speed stability and structural integrity [11].

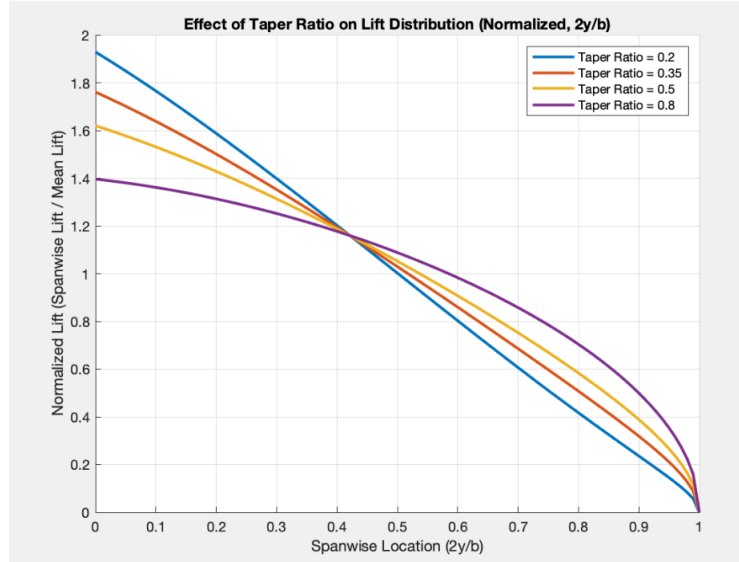


Figure 21: Normalized Lift Distribution for Various Taper Ratio

### 9.1.5 Wing Incidence And Twist

For fighter jets, a typical root incident angle is between  $1^\circ$  to  $2^\circ$ , which helps optimize our lift to drag ratio during high speed cruise, particularly in the supersonic segment. Our chosen low incident angle of 2 degrees reduces drag, which is essential for our design [12].

The twist or washout for a supersonic aircraft based on historical data ranges between  $-1^\circ$  to  $-3^\circ$ . For our chosen taper of 0.35, a  $-2^\circ$  twist was chosen to ensure that the wing tips have a lower angle of attack compared to the root. This will prevent tip stalling during low speeds segments of the mission such as takeoff and landing where the aircraft is more prone to instability. A small amount of twist will help us achieve more optimal lift and be closer to an elliptical lift distribution[13].

### 9.1.6 Sweep

The sweep angle is critical for our performance parameters because it aids in reducing drag considerably at supersonic speeds. Especially at transonic speeds—which we are hoping to optimize for—the wing sweep will mitigate the adverse drag from transonic flow and increase the speed at which shocks will begin to form. Introducing sweep will also increase our aircraft's lateral stability given our speed requirements and maneuverability constraints.

We began our derivation of sweep by utilizing a method established by Raymer [1] that allows us to estimate our quarter chord sweep from our determined aspect ratio, shown in Figure 22. This led us to choose a quarter chord sweep around 40 degrees from the transonic flight region.

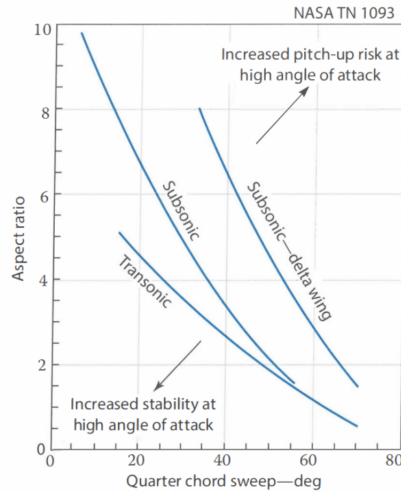


Figure 22: Determining the Quarter Chord Sweep from our Aspect Ratio

We then determined the leading edge sweep according to the following equation [1]:

$$\tan(\Lambda_{LE}) = \tan(\Lambda_{c/4}) + \frac{1 + \lambda}{AR \times (1 + \lambda)} \quad (7)$$

Where our aspect ratio ( $AR$ ) is defined as 3.6, the taper ratio ( $\lambda$ ) is equal to 0.35, and the quarter-chord sweep ( $\Lambda_{LE}$ ) is 35 degrees. This would then yield a leading edge sweep value of around 45 degrees.

We later verified our assumptions by ensuring that at this specific leading edge sweep, our wing remains in subsonic flow up to a speed of Mach 1.2, which is the speed we would see in combat and at various points throughout our mission profiles. This was derived from the component break down of the speed at the leading edge of the wing. We ensured that at the critical Mach number our wing remained behind the mach cone in order to prevent supersonic flow over the wing which would cause increased wave drag [14]. Given that our airfoil has a maximum thickness to chord ratio of 5 percent, we utilized historical trends from

Raymer [1], in figure 23, to attain a critical mach number of about 0.85 for our airfoil. This critical value was used in the component breakdown, to ensure that we remained below this value up to mach 1.2. After further refinement, we established our leading edge sweep to be 44.9 degrees.

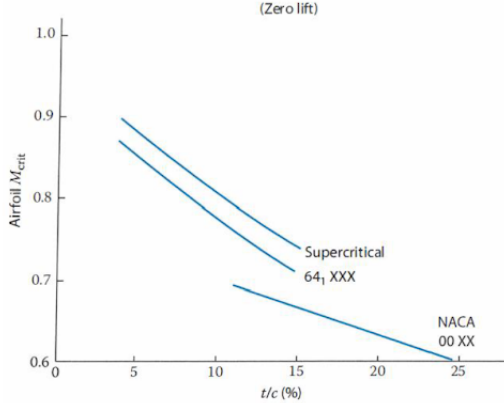


Figure 23: Critical Mach number as a function of Thickness Ratio

### 9.1.7 Wing Configuration

Our wing will be placed in a mid-wing configuration. This allows the wing to be streamlined with the fuselage to minimize interference drag at transonic speeds. This will also enhance performance during high G turns and rapid maneuvers. Mid-wings avoid ground clearance issues associated with low-wing designs and the over-stability in roll associated with high-wing configurations. Our wing is aligned with the center of gravity of the aircraft in order to reduce roll inertia [15].

Our wings will also be cantilevered. Braced wings produced far too much drag at high speeds to be feasible for the mission requirements we are tasked with. Our aircraft will also have a dihedral angle of 0°. We designed our aircraft with neutral stability in mind to ensure that it can quickly adapt to changing flight conditions as well as maintain sufficient control during cruise and combat. In general, these design parameters within the wing configuration allow for simpler and more cost-effective structural reinforcements, aligning with our primary objective of maintaining low cost while ensuring responsive control [15].

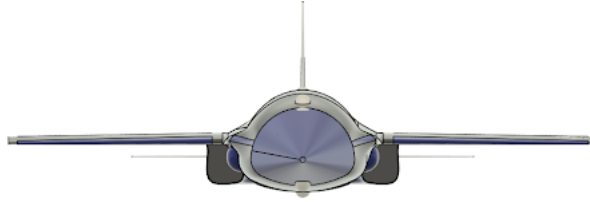


Figure 24: CAD Image of Libellula F-81's Wing Configuration

### 9.1.8 High Lift Devices

We incorporated leading-edge extensions (LEX) into the Libellula F-81's design to enhance its combat maneuverability and overall aerodynamic performance. These extensions significantly improve high-angle-of-attack behavior, generating lift-inducing vortices that delay stall and provide greater control during critical phases of flight such as takeoff, landing, and air combat [16]. While LEX may introduce some drag increase and pitch-up tendencies, these effects are far outweighed by the enhanced maneuverability they offer in dynamic combat scenarios. Additionally, LEX address the isobar unsweep problem at the wing root, opti-

mizing the pressure distribution and improving aerodynamic efficiency [1]. By aiding in the area ruling of the aircraft, they also contribute to reduced wave drag, enhancing the overall performance and versatility of the F-81 in high-speed operations. The LEX on the F-81 can be seen in figure 25 below.



Figure 25: Leading edge extensions on the Libellula F-81

The design also utilizes flaperons, combining flaps and ailerons into a single control surface. This integration offers significant advantages in terms of both cost and performance, simplifying the wing layout and reducing overall aircraft weight. The combined flaperon design provides the remote pilot with more precise control authority by unifying roll and lift management into one system. This control surface setup is also essential to counteract the reduced lift associated with our thin airfoil, ensuring adequate lift during takeoff and landing [16].

The flaperon sizing was initially based on guidelines from Raymer's textbook [1], with parameters including an aileron-to-wing chord ratio of 0.30, a span ratio of approximately 0.6, and a taper ratio of 0.75 to minimize additional wing weight. The equations and historical data used for the initial sizing of these specific sizing parameters can be found in the Appendix, Figures 54 and 55. After refining the aerodynamics of our aircraft, we later increased the size of the flaperons in order to increase the total amount of lift we were able to generate. In having a very thin airfoil that is optimized for the transonic flight regime, we wanted to ensure that we were still producing enough lift during low-speed flight. For this reason, we increased the size of our flaperons to span a larger portion of the wing.

The F-81 aircraft design also uses leading edge flaps to effectively increase the camber of the airfoil, enhancing lift during high angle of attack maneuvers and supporting additional lift during low-speed phases such as takeoff and landing. These flaps offer a straightforward design that helps to reduce weight and cost, making them easier to integrate into the aircraft's dynamic control system for combat scenarios. Unlike slats, leading edge flaps maintain a seamless airfoil shape that supports high-performance maneuvers without the increased drag that can result from slat gaps.

Utilizing an estimation method from the Raymer textbook [1], we can approximate the contributions of the flaperons and leading edge flaps to our total  $C_{L,max}$  value of the aircraft. This relation is shown below.

$$\Delta C_{L_{max}} = 0.9 \Delta C_{\ell_{max}} \left( \frac{S_{flapped}}{S_{ref}} \right) \cos \Lambda_{H.L.} \quad (8)$$

Given that our reference area is  $25.25 m^2$ , and the changes in the 2 dimensional lift coefficient can be approximated by historical data from the Raymer textbook (figure 26), we are able to estimate the additional lift contributions from both the flaperons and the leading edge flaps. Therefore, the flaps provide an additional contribution of 0.394 to the total  $C_{L,max}$  of the aircraft, given that they span 30 percent of the chord length, have a flapped area of  $14.46 m^2$ , and a hinge-line sweep of 31.8 degrees. The leading edge flaps span 10 percent of the chord length, have a flapped area of  $14.46 m^2$ , a hinge-line sweep of 43.3 degrees and provide an additional 0.113 increase in  $C_{L,max}$  according to equation 8.

High-lift Device	$\Delta C_{l_{\max}}$
<b>Flaps</b>	
Plain and split	0.9
Slotted	1.3
Fowler	$1.3 c'/c$
Double slotted	$1.6 c'/c$
Triple slotted	$1.9 c'/c$
<b>Leading-edge devices</b>	
Fixed slot	0.2
Leading-edge flap	0.3
Kruger flap	0.3
Slat	$0.4 c'/c$

Figure 26: Approximate contributions for lift from high lift devices [1]

## 9.2 Wing Airfoil Selection

PDR feedback on our initial selection of a NACA 6-series laminar flow airfoil motivated a selection based on airfoil aerodynamics fundamentals and our prioritized flight regimes – cruise and dash. The SC(2)0606 met our criteria due to its thin ( $6\% \frac{t}{c}$ ) supercritical profile that would allow shock delay during cruise and weaken oblique shocks during dash. Furthermore, the airfoil has been shown to provide stability at high angles of attack while preserving lift [17]. However, the initial CFD analysis showed undesirable bow shock formation at our root and mean airfoils’ leading edges (simulated by carefully selecting the simulation’s Reynolds number) and strong shocks at our trailing edge. Therefore, we chose to feed the SC(2)0606 shape to an optimization software with an instruction to minimize drag at our chord-wise mach number during dash and have a  $C_l$  of 0.3. We hoped that the airfoil would retain its properties in the transonic regime due to the input shape provided to the optimizer; however, the resulting airfoil seen in Fig. 27 a possessed an insufficient  $C_l$  of 0.345 at cruise. An additional optimization point with the required lift coefficient at cruise was then added resulting in the profile seen in 27 b.

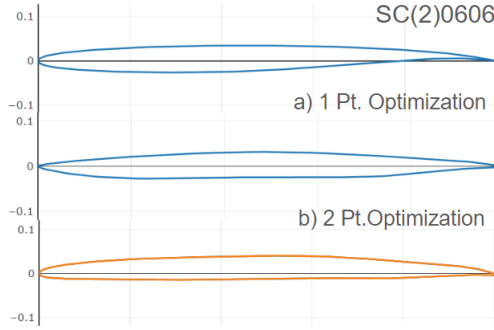


Figure 27: Wing Airfoil Optimization Input and Results

Table 8: Optimizer Input Values

Opt. pt. 1	Opt. pt. 1	Cd Weighting
$M = 1.13$	$M = 0.6$	0.65 @ 1
$Cl = 0.3$	$Cl = 0.7$	0.35 @ 2
$AoA = 2^\circ$	$AoA = 2^\circ$	

Looking closer at the airfoil’s lift distribution when oriented at an incidence of 2 degrees, the airfoil

generates its leading edge lift through a gradual increase in thickness to chord meant to align tangentially to the flow. Lift is maintained with relatively constancy as flow moves aft of the airfoil, with an additional small increase near  $\frac{3*c}{4}$  as the trailing edge forms (Fig.28). A cusp is also visible on the bottom surface of the trailing edge for additional lift to compensate for the pressure recovery on the top surface (Fig.28). Optimization software inputs may be seen in table ???. This airfoil not only produces sufficient lift at cruise but also has a high drag divergence mach number (Fig. 29) at 0.95 Mach, resulting in a critical mach number value of 0.84 Mach for the entire wing.

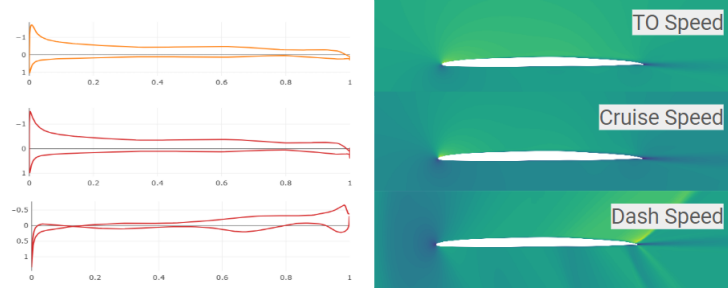


Figure 28: Wing Airfoil Performance at Primary Flight Speeds

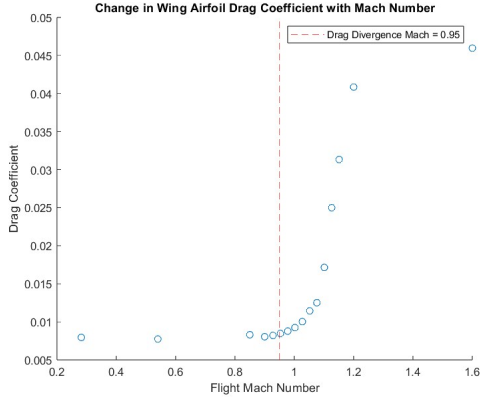


Figure 29: Change in Wing Airfoil Drag Coefficient with Angle of Attack

Our custom airfoil's thin profile comes with some downsides. It's unable to generate sufficient lift without the 2 degree incidence which inherently increases drag. Furthermore it has a small stall margin -visible in Fig. 30, only being able to reach angles of attack greater than  $10^\circ$ ( $8^\circ$  aircraft pitch) above  $M = 1.2$ . While this is promising for our highest speed maneuver, it indicates that leading and trailing edge flaps are necessary for all other maneuvers including take off and landing.

### 9.3 Stall Speed

To calculate the stall speed of the aircraft, we utilized a method following the design process of past aircraft. With the relation provided in equation 9 [1], we can input parameters from our aircraft to yield an estimate of the velocity we will experience stall at. With a  $C_{L,max}$  of 0.89 in the aircraft's takeoff configuration, a  $W_0$  of 13,882.19 kg multiplied by  $g = 9.81 \text{ m/s}^2$  (provided that takeoff weight will yield the most critical case),  $S_{ref}$  of  $25.25 \text{ m}^2$ , and  $\rho$  of  $1.225 \frac{\text{kg}}{\text{m}^3}$  at sea-level, we attained a stall speed velocity of approximately 99.47 m/s. We believe that this is a reasonable stall speed for our aircraft, as most fighter aircraft have a stall speed ranging from about 70-110 m/s.

$$V_{stall} = \sqrt{\left(\frac{2}{\rho \times C_{L,max}}\right) \times \left(\frac{W_0}{S_{ref}}\right)} \quad (9)$$

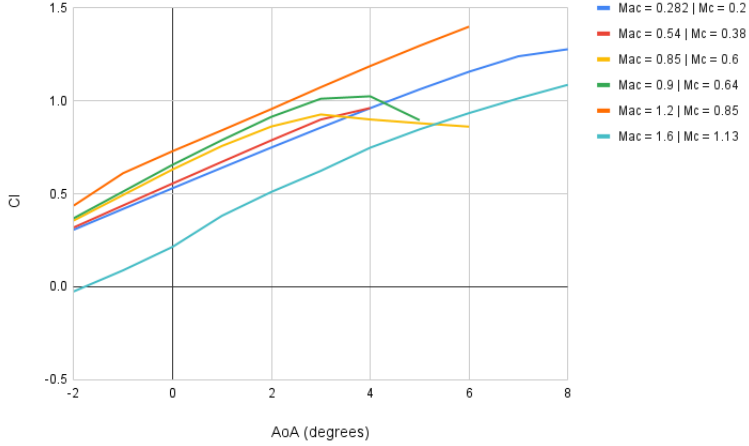


Figure 30: Change in Wing Airfoil Lift Coefficient v.s. Angle of Attack at Mission Flight Speeds

## 9.4 Empennage Configuration

### 9.4.1 Vertical Tail

After removing our top-mounted engine inlet we were able to simplify our vertical tail's placement on the fuselage by using a single tail configuration. Although this increases the load concentration on top of the engine and removed the possibility of using the horizontal tail's structure to carry the loads of the vertical tail, a single tail reduces the number of actuators needed for lateral control which translates into less parts requiring maintenance and a decrease in our operating cost. An additional benefit comes from the potential to align our aft camera with the highly swept (and therefore gradually sloping) vertical tail leading edge to induce turbulence on the stabilizer's leading edge that could help keep the flow onto our rudder's root clean. We have not been able to verify this design feature yet since simulating it would require using large eddy simulation, which our team members currently don't know how to perform.

The vertical tail was swept by  $\Lambda = 55^\circ$  following historical data from Raymer [1]. This number was verified by identifying a chord-wise Mach number of 0.918 at our maximum speed of  $M = 1.6$  using equation 10.

$$M_{chord} = M_{freestream} \cos(\Lambda_{VT}) \quad (10)$$

This shows that our airfoil will largely see transonic speeds during the dash phase. Transonic flow allows us to delay shockwave formation and reduce wave drag while also trending toward a high enough Mach number at our maximum thickness to chord point ( $\approx 0.5c$ ). This will help maintain subsonic flow onto the rudder, which begins at  $0.7c$  and extends to the trailing edge. An aspect ratio of  $AR = 2$  was selected to reduce the induced drag affecting the rudder, which will be placed at the vertical tail's root. This value is on the higher end for fighters according to Raymer Table 9.3 [1].

Raymer Table 6.5 [1] shows that fighter jet rudders typically extend to 30% of the vertical tail's span. Our design proceeded with the assumption that this value can be used for both single and dual tail configurations given that the same total lift must be produced to control the aircraft. A preliminary lift distribution analysis was conducted with the same methodology used in section 9.1.4 for the wing taper. We selected a taper of  $\lambda = 0.35$  given that its high value will help reduce induced drag. This led us to choose to extend our rudder span to 38% of the tail to capture  $\approx 50\%$  of the lift produced by the tail as seen in Figure 33.

### 9.4.2 Horizontal Tail

As mentioned in section 8, our aircraft will be stable during takeoff (low speed) and unstable during cruise (transonic speeds) and dash (supersonic speeds). This requires an all-moving horizontal stabilizer as

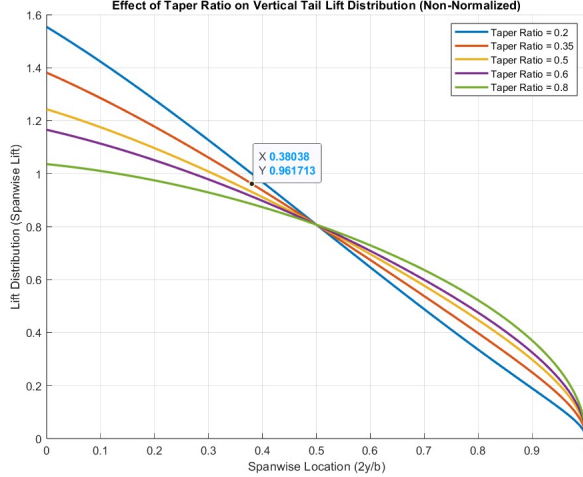


Figure 31: Non-Normalized Lift Distribution on Vertical Tail with Varying Taper Ratios

fuel is expended with control authority at all speeds and therefore very careful airfoil selection and design, which will be expanded on in section 9.5.

The horizontal tail's sweep and placement were determined to ensure that it stalls after the wing. This included sweeping the leading edge by  $5^\circ$  or  $\approx 11\%$  more than the leading edge of the wing, resulting in a final sweep of  $\Lambda = 49.89$ . This was done because a lower chord-wise Mach number will reduce the probability of flow separation. The horizontal tail's placement was guided by a chart built from an experimental study conducted by NACA [18] that guides a tail's vertical placement ( $\frac{\Delta z}{c}$ ) with respect to the x-z coordinates of the wing's M.A.C. depending on  $\frac{x_{tailarm}}{c}$ . This value was calculated using the following equation 11.

$$\frac{x_{tailarm}}{c} = \frac{x_{MAC_{wing}} - x_{MAC_{tail}}}{c} \quad (11)$$

A margin of approximately  $-0.1(\frac{z}{c})$  was added to the minimum allowable vertical distance. This resulted in  $\frac{\Delta z}{c} = -0.2$ ,  $\Delta z = -0.6096m$  after a careful visual inspection of Figure 3 in [18].

We aim to have a lift-efficient horizontal stabilizer due to the low lift that thin airfoils produce at takeoff. This led to an aspect ratio selection of  $AR = 4$ , which remains within the bounds of historical values listed in Raymer Table 6.4 [1]. Our taper ratio analysis showed that a value of  $\lambda = 0.5$  would get us fairly close to an elliptical lift distribution while still allowing us to utilize our high aspect ratio. The following lift distribution may be found in the appendix as Figure 59.

Our airfoil selection and consequent analysis of  $\frac{\partial C_{L_h}}{\partial \alpha}$  shown in section 9.5 will provide more clarity on the horizontal stabilizer's effect on longitudinal stability.

## 9.5 Empennage Airfoil Selection

### 9.5.1 Vertical Tail

A biconvex airfoil with a 3.3% thickness to chord ratio was selected due to its sharp leading edge and gradual increase in thickness along its chord. The sharp leading edge will allow optimal performance at supersonic speeds given that it will generate an oblique shock that will slow down the flow coming onto the rudder. This airfoil provides a nice balance between shock delay and allowing space for subsonic flow into our control surfaces when assuming that in the transonic regime the shock will form at the maximum  $\frac{t}{c}$  location (0.5c for a biconvex airfoil).

### 9.5.2 Horizontal Tail

The horizontal tail airfoil poses an interesting challenge given that it must produce sufficient lift to rotate during takeoff, provide a controlling force at both positive and negative incidence angles -given our transition from stable to unstable during flight- and minimize wave drag. These considerations lead to design constraints such as symmetry, and low  $\frac{t}{c}$ . While the biconvex airfoil has both the symmetry that our aircraft's varying stability requires, low  $\frac{t}{c}$  and the gradual thickness increases that will allow for a gradual shock development along its chord it has terrible lift production at low speeds. Viscous vortex panel simulations were unsuccessfully attempted on this airfoil, given that these simulators are meant to be used on airfoils with rounded leading edges. Hence, a lift curve slope analysis was performed on NACA 0003 as a very rough estimate for the properties of an airfoil of similar thickness and symmetry.



Figure 32: Custom Airfoil Used for the Horizontail Stabilizer

These were the conclusions drawn at the end of the Preliminary Design Review, however, since then we have incorporated a custom airfoil made using Mach Aero that optimizes the NACA 0006 airfoil and allows our aircraft to reach our ideal  $C_l$  values for takeoff and landing conditions. These  $C_l$  values are laid out in table 16.

Opt. pt. 1	Opt. pt. 2	Opt. pt. 3	Cd Weighting
M = 0.182	M = 0.38	M = 1.091	0.15 @ 1
$C_l = 0.9$	$C_l = 0.7$	$C_l = 0.3$	0.5 @ 2
AoA = -8 degrees	AoA = 0 degrees	AoA = 3 degrees	0.35 @ 3

Table 9: Airfoil Shape Optimized by Ideal  $C_l$  Values

## 9.6 Dimensions After Volume Coefficient Based Sizing and Airfoil Selection

Volume coefficients were taken from historical values in Raymer Table 6.4 [1]. Consequently, our horizontal tail volume coefficient  $c_{HT} = 0.4$  and our vertical tail volume coefficient came out to  $c_{VT} = 0.07$ . This allowed us to solve for both tails' platform areas and obtain our geometric parameters by following the same sizing process as the wing. These parameters are listed in Table 26 in the appendix (section XV).

## 9.7 Refined Drag Estimates

To find refined drag polars, we used the component build up method detailed in Lecture 14 - Aerodynamic refinement. We were unable to get accurate values for wave or trim drag in time, so our drag polars are only parabolic functions of  $C_L$  and our  $C_{D0}$  from the component buildup.

Flight Condition	$C_L$
Takeoff Clean	0.47
Cruise	0.56
Takeoff (Flaps + Slats)	0.88
Landing (Flaps + Slats)	1.35

Table 10:  $C_L$  Values for Different Flight Conditions from 2D airfoil CFD

Flight Condition	$C_{D0}$
Cruise	0.020556400403123
Takeoff (Flaps + Slats)	0.033
Takeoff (Flaps + Slats + Gear)	0.048
Landing (Flaps + Slats)	0.070
Landing (Flaps + Slats + Gear)	0.085

Table 11:  $C_{D0}$  Values for Different Flight Conditions from component buildup

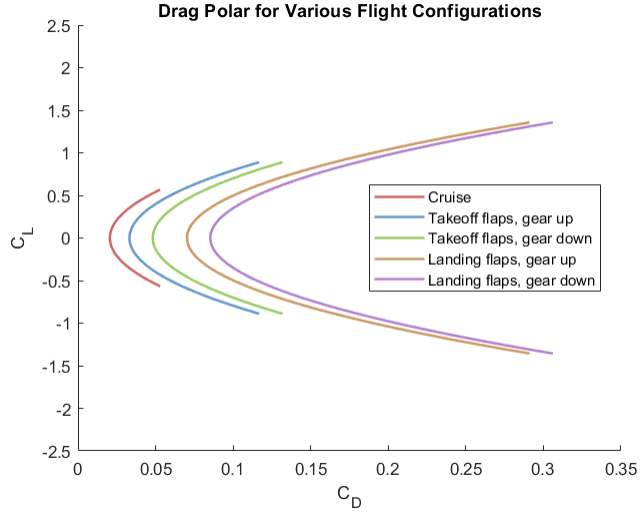


Figure 33: Parabolic drag polar using only refined  $C_{D0}$  and  $C_L$  values from airfoil CFD

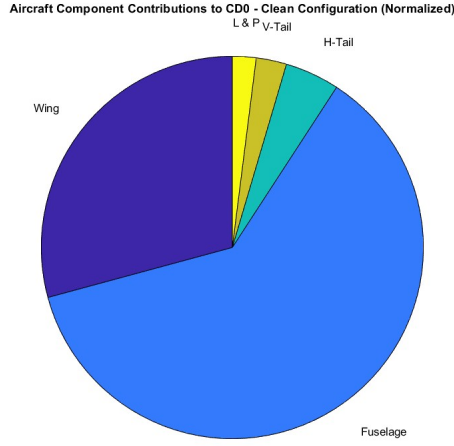


Figure 34: Contributions Of Different Components to Parasitic Drag

## 10 Objective Function

As outlined in the RFP, this interceptor will address the need for an affordable aircraft within the US Air Force and Navy fleets. The F-35 and F-22, designed for air superiority, are too costly to be procured in

the quantities required to strengthen US defense amid rising international political tensions. Consequently, our aircraft should be as inexpensive as possible while meeting all other operational capabilities, and have defined cost as our objective function. We must provide 1,000 aircraft to fulfill our contract.

## 10.1 RTD&E and Flyaway Cost

As a preliminary estimate for flyaway cost, we utilized method A13 in Roskam's Airplane Design [19] Section 8, Appendix A for calculating the flyaway cost of a military aircraft as a function of TOGW:

$$\text{cost}_{1989} = 10^{2.3341 + 1.0586 \cdot \log_{10}(\text{Wto})} \quad (12)$$

This gives us a rough estimate of the flyaway cost in 1989, which we adjusted for inflation following 20.1.1.

This initial estimate provides confidence that the F-81 is appropriately sized given the cost constraint of \$25 million; This method yielded an initial average flyaway cost of \$14.6 million per aircraft for 1000 aircraft with the preliminary estimated TOGW of 12,500 kg.

To refine our cost estimates, we used the RAND DAPCA IV cost estimation relation (CER) given in Raymer [1] section 18.4.2. The DAPCA IV CER is used to calculate the combined research, development, test, and evaluation (RTD&E) and flyaway costs for a given program. These relations are functions of aircraft empty weight, maximum flight velocity (EAS), and production quantity, and calculate:

- Engineering hours
- Tooling hours
- Manufacturing hours
- Quality control hours
- Development support cost
- Flight test campaign cost
- Manufacturing materials cost

DAPCA IV's method for engine cost was not utilized, as we had already selected the F110-FE-132. The cost of avionics is not included in this CER, and must be estimated separately.

The number of manufacturing and quality control hours were adjusted using a 95% learning curve (see section 20.1.2 for details on this adjustment) to account for improvements in the manufacturing process as more aircraft are produced and the assembly line becomes more efficient. As manufacturing technologies improve, early program production is more efficient and closer to optimal efficiency. Consequently, 95% was selected so as to not overestimate this efficiency gain. Each of these man hour calculations was multiplied by a fudge factor of 1.8. This fudge factor corresponds to the more complicated nature of manufacturing with composites, which is the lightest, most high-performing class of structural material today. Consequently, manufacturing, quality control, tooling, and engineering is expected to take 1.8 times longer.

Each of these hour totals was multiplied by the hourly rate of labor given in Raymer 18.4.2 [1], adjusted for inflation.

An estimated 6 flight test aircraft was selected to calculate the flight test campaign cost. This was the upper limit given in Raymer, and was selected due to the experimental nature of our program - a fully remote interceptor of the F-81's size and mission does not yet exist.

The cost of the F-81's engine, the F110-GE-132, was estimated using a GE press release [20], by dividing the total contract cost by the number of requested engines and adjusting for inflation, yielding a cost per engine of \$7.77 million.

The cost of avionics was set to 40% of the totaled program, which was the upper limit of avionics cost given by Roskam, Part 8 [21], Appendix C2. We chose the highest value for avionics cost because our aircraft is operated fully remotely which is novel for an aircraft of the F-81's size and mission. Consequently, the development and production of avionics and software advanced enough to engage in remote combat will constitute a large portion of the total program cost.

To calculate the average cost per aircraft, the total RTD&E + flyaway cost was divided by  $Q$ . The average cost per aircraft to produce 250, 600, and 1000 aircraft given an empty weight of 7560 kg and maximum flight velocity (EAS) of 264 m/s are displayed in Table 12.

Table 12: Average Flyaway Cost by Quantity Produced

$Q$	Avg. Flyaway Cost
250	\$31.6 M
600	\$24.8 M
1000	\$22.3 M

As shown in Table 12, our aircraft meets the \$25 million requirement when approximately 600 aircraft are produced (which is why we included this quantity above for convenience). When 1000 units are produced, the average cost per aircraft is well below this requirement, at \$22.3 million (program cost \$22.3 billion). A breakdown of each cost component is shown in Table 13, and visualized in Figure 35.

Category	Cost (Billion \$USD)
Engines	7.77
Engineering	0.61
Tooling	0.57
Manufacturing	2.55
Quality Control	0.67
Development Support	0.03
Flight Test	0.04
Manufacturing Material	1.13
Avionics	8.92
<b>Total</b>	<b>22.30</b>

Table 13: Cost Breakdown by Category in Billions of USD

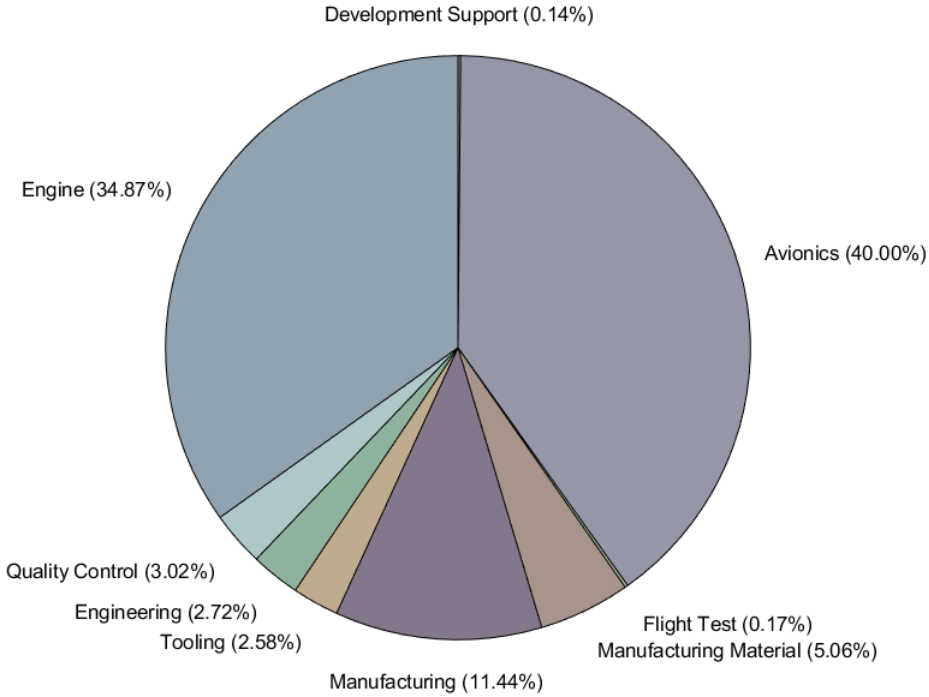


Figure 35: Program RTD&E and Flyaway Costs Breakdown

## 10.2 Operating Cost

To calculate the total operating cost of all F-81 aircraft over the program years in service, the methods presented in Roskam, Part 8 [21], section 6 were used without modification. Roskam defines operating cost in terms of 7 components, which we calculated separately and added to get the total program operating cost:

- Fuel, oil, and lubricant
- Direct personnel (flight and maintenance crew)
- Indirect personnel (other squadron personnel associated with operation)
- Consumed materials in maintenance
- Spares
- Depot (overhaul and maintenance not at the squadron level)
- Miscellaneous

A few key parameters were regarding the program life cycle were selected that factor heavily into the total program operations cost, as seen in Table 14

Parameter	Value	Rationale
Mission block time in hours	6.60	Calculated from our model of the DCA mission, combining historical values with products of cruise/dash distanced with flight velocities
Flight hours per aircraft per year	350	Selected as the average value given in Roskam Table 6.1.
Number of reserve aircraft	10%	Given by Roskam equation 6.7 for preliminary estimates.
Number of aircraft in service	790	Calculated from Roskam equation 6.4.
Number of years in service	40	Upper limit of range provided by Roskam section 6.1, as newer aircraft are designed to be more robust and will have more longevity.
Annual loss rate per $10^5$ hours	2.0	Slightly above the average value for military aircraft provided by table 6.2.
Number of crew	2	The General Atomics MQ-9 Reaper, a currently operational remote attack aircraft, has two crew: a pilot and sensors operator. We will assume a similar configuration for our aircraft control
Crew ratio per airplane	1.1	Average number for fighters taken from Roskam table 6.1
Maintenance man hours per flight hour	35	The upper limit of the range for fighters provided by table 6.5. This newer, more complicated aircraft will take longer to service.
Spares cost fraction	0.168	The average number across all aircraft provided by table 6.6
Depot cost fraction	0.172	The average number across all aircraft provided by table 6.6
Indirect personnel cost fraction	0.170	The average number across all aircraft provided by table 6.6

Table 14: Operational and Maintenance Parameters with Rationale

One key simplification was made in the calculation of program operating cost: All missions flown will be the most demanding- the DCA mission. Although this will likely not be reality, we decided to overestimate our direct operating cost in this way to provide margin for program costs that will inevitably increase in as the program develops. A breakdown of each of these costs is shown in 15 and visualized in 36

Category	Cost (Billion \$USD)
Fuel, Oil, Lubricant	9.57
Direct Personnel	55.72
Consumable Materials	5.24
Miscellaneous	20.97
Indirect Personnel	31.75
Spares	31.37
Depot	32.12
<b>Total</b>	<b>186.74</b>

Table 15: Operational Costs Breakdown in Billions of USD

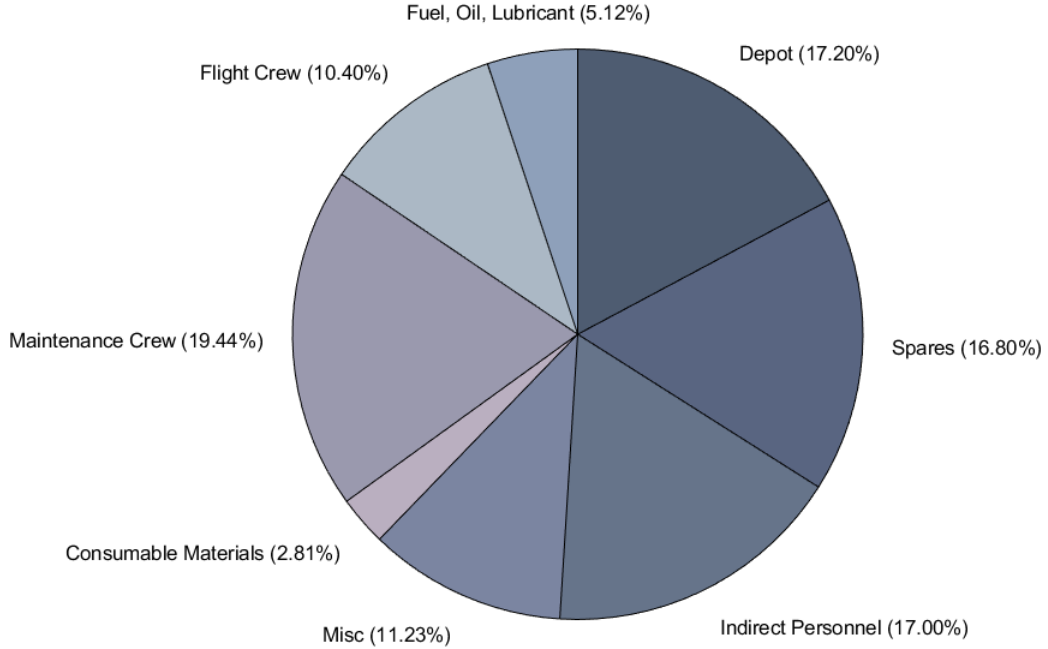


Figure 36: Program Operation Costs Breakdown

Multiplying our selected service life, the number of flight hours per aircraft per year, and the number of aircraft in service yields the total number of service hours for the F-81 over the program lifetime: 11 million hours. Dividing total operating cost by this value yields an **operating cost per hour of \$16,900**, far less than the operating cost of the F-22, which is approximately \$60-80,000 per flight hour [22]. This confirms that our aircraft serves its purpose as a cheaper alternative to current active fighters as requested by the RFP.

## 11 Propulsion System

The engine selected for our aircraft is the F110-GE-132 (shown in Figure 37). This provides 144.6kN of thrust at MAX throttle and 84.5kN at MIL throttle, matching the thrust requirements discussed in the sizing section above. This is the next iteration of our last engine choice, the F110-GE-132, upgraded as it was observed that the increased weight of the aircraft drove thrust requirements up. No changes to the geometric parameters were necessary. With a legacy of being applied on the F-15E and later versions of the F-16, the engine was deemed to be the best choice in terms of value and performance. A dual engine configuration necessitated a larger cross-sectional area of the fuselage especially towards the rear of the aircraft and a larger flow rate which would also inevitably contribute to the general size of the aircraft. Even if a single engine configuration puts our aircraft significantly below the thrust levels of 4+ to 5th generation fighters currently in service today, our high T/W ratio as well as the maneuverability considerations will help our aircraft be competitive in combat. The unit price of a single F110-GE-132 is taken to be \$7.77 million.

The engine inlet was redesigned to be located beneath the wings of the aircraft, in a dual-inlet, scarf'd channel design that combines the flow from both inlets seamlessly in the diffusion section just upstream of the engine. As discussed before, it was unclear with such little documentation and implementation examples whether the design would be feasible in the context of a supersonic interceptor. To reduce the additional costs of utilizing new or untested technology in our aircraft, we have decided to implement a much more conventional form of inlet. Figure 38 shows a view of the aircraft from below, which better shows the nature

of the inlets. The curved ducts still raise concerns regarding pressure recovery and unstable flow into the engine, but enough testing and analysis has been done on this type of inlet, and is actively applied by several aircraft such as the Boeing-Saab T-7A and the KAI T-50 Golden Eagle. The bulges ahead of the openings of the ducts are shock humps that helps to turn boundary layer air away from the inlet by creating a region of high pressure.

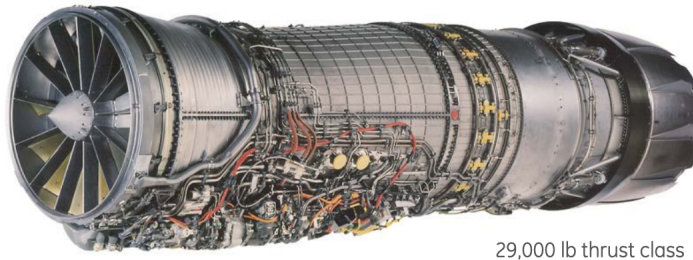


Figure 37: F110-GE-132 Engine Selection



Figure 38: Image of the underside of the aircraft, showing a better view of the engine inlets.

## 12 Government Furnished Equipment

As outlined in the Homeland Defense Interceptor RFP, Government Furnished Equipment (GFE) was used to the furthest extent. A list of all GFE available and our rationale is shown in the following list and in Figure 39.

1. **Integrated Communication, Navigation, and Identification Avionics:** Included; fundamental avionics equipment necessary especially as an uncrewed aircraft.
2. **Multifunctional Displays:** Not included; MFDs not needed onboard in the absence of a pilot.
3. **Head-Up Display:** Not included; HUDs not needed onboard in the absence of a pilot.
4. **Data Bus:** Included; effective aircraft data and telemetry handling is crucial for an unmanned system.
5. **Integrated Electronic Warfare System:** Included; in the event of retaliation by intercepted enemy aircraft, effective deterrence and defensive countermeasures are not only desired, but also necessary.
6. **Vehicle Management System:** Included; aircraft health is much more difficult to assess as a ground operator; the VMS can handle and deliver such crucial information to the operator.

7. **Infra-Red Search and Track System:** Included; a passive method of target tracking, even in the absence of heat-seeking infrared guided missiles to complement, can greatly contribute to surprising enemy aircraft.
8. **Active Array Radar:** Included; fundamental avionics needed to track targets at long range and lock targets for AMRAAMs.
9. **Engine Electrical System:** Included; FADEC control and related electrical subsystems critical to effective engine control.
10. **Auxiliary Power Unit:** Included; APU needed for startup or emergency engine restart during flight.
11. **Onboard Oxygen Generation System:** Not included; not needed onboard in the absence of a pilot.
12. **Onboard Inert Gas Generation System:** Not included; although higher fuel volume increases risk of fires, ultimately serves to take up more space to reach all fuel tanks around the aircraft. An alternative solution of using self-sealing fuel tanks should be pursued.
13. **AIM-120 AMRAAM:** Included; part of the basic weapons load, effective in beyond visual range (BVR) combat.
14. **M61A1 Cannon:** Included; part of the basic weapons load, more useful in extremely close-quarters combat.

A justification of how each GFE achieves the HDI design requirements is listed below. The design requirements of the aircraft are listed and labeled, for ease of referencing in our justifications.

## Requirements

1. **Design a homeland defense interceptor, including an engine data package.**
2. **The design should be cost effective and perform three design missions.**
  - (a) A defensive counter-air (DCA) patrol mission will be evaluated.
  - (b) A point defense interception mission will be evaluated.
  - (c) An intercept/escort mission will be evaluated. Attachment 3 provides specific information.
3. Attachment 4 specifies minimum performance requirements.
4. Attachment 5 specifies weapons carriage capabilities.
5. Attachment 6 specifies engine design requirements.

## Miscellaneous Requirements

1. **Remote Pilot (required):** All systems must be designed for remote pilot operation. The pilot can control the aircraft remotely if the operational concept accomplishes positive threat identification and clearly addresses all communication bandwidth issues. An unmanned approach can remove any man/machine interfaces from the aircraft, but must address remotely piloted infrastructure issues in full detail.
2. **Maintenance (required):** The design must allow easy access to and removal of primary elements of all major systems. Minimize requirements for unique support equipment.
3. **Structure (required):** Design limit load factors are +7 and -3 vertical g's in the clean configuration with 50% internal fuel. The structure should withstand a dynamic pressure of 2,133 psf ( $M=1.2$  at sea level). A factor of safety of 1.5 shall be used on all design ultimate loads. Primary structures should be designed for durability and damage tolerance. Design service life is 2,000 hours.

4. **Fuel/Fuel Tanks (required):** Primary design fuel is standard JP-8 or Jet-A (6.7 lb/gal). All fuel tanks will be self-sealing. External fuel tanks may be carried for design missions, but if carried, must be retained for the entire mission.
5. **Stability (required):** Unaugmented subsonic longitudinal static margin (S.M.) shall be no greater than 10% and no less than -10%. A digital flight control system is mandatory for designs that are statically unstable in the longitudinal axis.
6. **Operation (required):** The aircraft must operate in all weather from existing NATO runways (8,000 ft), shelters, and maintenance facilities and from austere bases without support equipment. The aircraft must be capable of all-weather interception and weapon delivery.
7. **Cost (required):** Flyaway cost per aircraft for a 1000 aircraft buy will not exceed \$25 million in 2024 US dollars. All practical measures will be taken to minimize total life cycle costs.

## System Components

1. **ICNIA:** Satisfies requirements 1.2 and 3.1. Fundamental avionics equipment required for all missions, especially for friend-or-foe identification and situational awareness (1.2); also facilitates remote pilot operations in awareness of position, unhindered communication, and target acquisition.
2. **Data bus:** Satisfies requirement 3.1. Facilitates communication between all electrical components within the aircraft, including fly-by-wire components, engine data from the FADEC, and warning, caution, and advisory information.
3. **Integrated Electronic Warfare System (INEWS):** Satisfies requirements 1.2 and 3.1. Essential for PDI and DCA missions; includes Radar Warning Receiver (RWR) and Missile Approach Warning System (MAWS) for enhanced awareness and faster response times, supporting automatic countermeasure firing.
4. **VMS:** Satisfies requirements 3.1 and 3.6. Allows monitoring of aircraft health, supporting decision-making even without a pilot in the cockpit, and facilitates diagnostics, eliminating the need for complex support equipment.
5. **IRSTS:** Satisfies requirements 1.2 and 3.1. Expands short-range engagement capabilities with passive target tracking and complements the AESA radar.
6. **AESA:** Satisfies requirements 1.2, 1.4, and 3.1. Essential for target identification and engagement, enabling Beyond Visual Range capabilities and AMRAAM missile locking.
7. **Engine Electrical System:** Satisfies requirement 3.1. FADEC and electronics ensure efficient engine operation, monitoring, and control across all flight states.
8. **Auxiliary Power Unit (APU):** Satisfies requirement 3.6. Provides self-start capability and allows the aircraft to operate in poorly-equipped airfields or quickly restart engines in-flight.
9. **AIM-120 AMRAAM:** Satisfies requirements 1.2 and 1.4. Essential for medium-to-long-range target engagement, using its own radar for "fire-and-forget" launches.
10. **M61A1 20mm Cannon:** Satisfies requirements 1.2 and 1.4. Used for short-range engagements, paired with IRSTS for precise target tracking.

For more information on the interior layout of these equipment, reference figures 13 and 14 in section 6.2 of this report.

	Equipment	Quantity	Volume [m³]	Weight [kg]	Cost [2024 USD]
Avionics	ICNIA	1	0.279	45.359	315.8K
	Data Bus	1	0.046	4.536	15.8K
	INEWS	1	0.279	45.359	789.6K
	HD45-LV-CV Gimbal	4	0.026	1.28	55K
Flight & Propulsion Control System	Vehicle Management System	1	0.093	22.680	315.8K
Fire Control Systems	IRSTS	1	0.186	22.680	315.8K
	Active Array Radar	1	0.557	204.117	1579.2K
Systems & Equipment	Electrical System (for 1 engine)	1	0.279	99.790	66.3K
	Auxiliary Power Unit	1	0.186	45.359	79.0K
Air-to-Air Weapons	AIM-120 AMRAAM	4	0.096	148.325	874K
	M61A1 20mm Cannon & Feed System	1	0.296	260.816	418K
Total			2.689	1349.116	7.61M

Figure 39: Table Indicating GFE and Relevant Parameters

## 13 Landing Gear

### 13.1 Sizing

The landing gear of the aircraft were placed such that all clearance angles would be satisfied without the need for a complex, oversized gear assembly that could be challenging to house in the fuselage. The landing gear, as determined in the preliminary design, were placed such that the lowest point of the aircraft would sit around 1.024 m off the ground. The main gear were placed 2.823 m apart when extended, symmetrical across the aircraft centerline. The nose landing gear was placed 4 m from the nose of the aircraft, and the main landing gear 10.196 m. This results in clearance angles as discussed in table 1, cross-referenced with the position of the center of gravity along the length of the aircraft.

Deeper analysis was conducted in the longitudinal direction with regards to the loads distribution among the nose and main gears. Figure 40 shows the relative lengths between the contact points of the main and nose gears and the centers of gravity at the maximum forward and backward positions. Raymer [1] recommends that to ensure the load on either gear is not too excessive, the ratio of the length between the main landing gear and the rearmost-possible center of gravity and the distance between gears ( $M_a/B$ ) must be no less than 0.05. Additionally, the ratio of the length between the main landing gear and the forwardmost-possible center of gravity and distance between gears ( $M_f/H$ ) should be no greater than 0.2. From the figure, we see that  $M_a/B = 0.07$  and  $M_f/H = 0.155$ , thus satisfying both constraints.

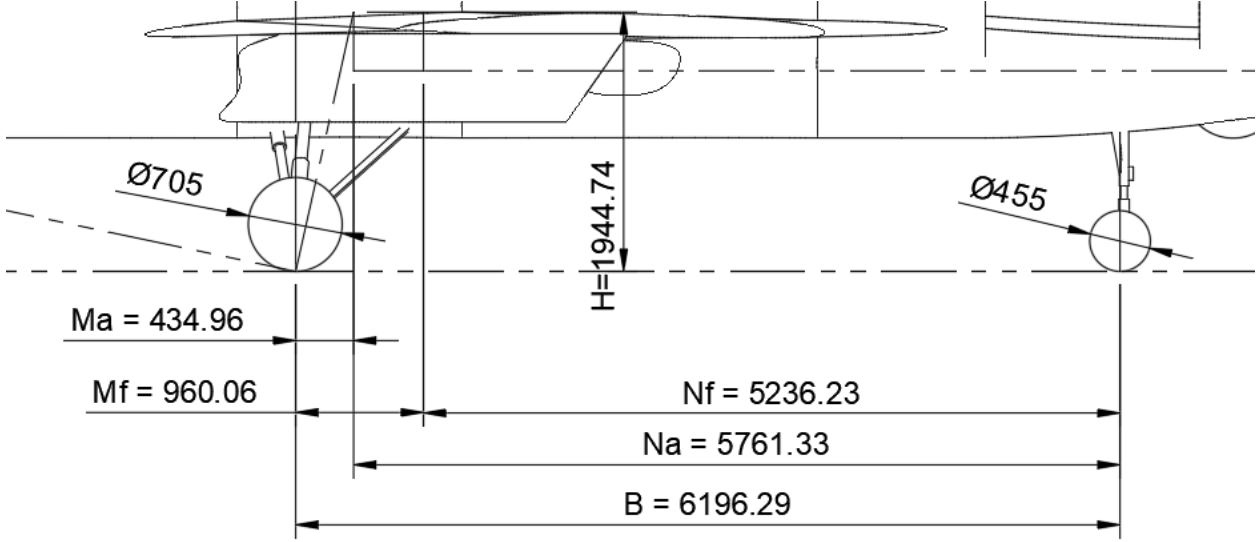


Figure 40: Relative lengths between landing gear contact points and extremities of centers of gravity.

Calculation of sustained static loads of the landing gear, assuming a total aircraft mass load of  $W = W_0 = 12500kg$ , can be calculated by equations 13 to 15:

$$SL_{nose,max} = W \frac{M_f}{B} = 1936.76kg = 4270lb \quad (13)$$

$$SL_{main,max} = W \frac{N_a}{B} = 11622.54kg = 25624lb \quad (14)$$

$$SL_{nose,min} = W \frac{M_a}{B} = 877.47kg = 1935lb \quad (15)$$

### 13.2 Landing Gear Choice

Based on these values, a "tire book" from Goodyear was consulted to find the optimal tire size for the sustained loads. With two main gear wheels, one on each side of the aircraft, the main landing gear was chosen to be of type 461B-3434-TL, while the nose landing gear was chosen to be 461B-3537-TL; the specifications for both tires are shown in table 16.

Parameter	461B-3434-TL	461B-3537-TL
Rated speed	250mph	225mph
Rated load	9000lb	21500lb
Rated inflation	315psi	320psi
Max diameter	17.9in	27.75in
Max width	5.7in	8.75in

Table 16: Tire specifications

With a 25% margin on all loads considering weight buildup, and for safety, the required rated load for both gears are  $SL_{main} = 32030lb$  and  $SL_{nose} = 5337.5lb$ . Two of the 27.75x8.75in tires completely satisfy the main gear load requirement, and one of the 18x5.7in tires satisfies the nose gear load requirement. However, to provide some margin in the kinetic energy dissipation of the brakes during landing, as well as to address the dynamic braking load, it was deemed appropriate to reinforce the nose landing gear with a dual nose wheel configuration. The final decision was to have two 461B-3434-TL tires for a dual nose landing gear and two 461B-3537-TL tires for the main gear, one for each side of the aircraft.

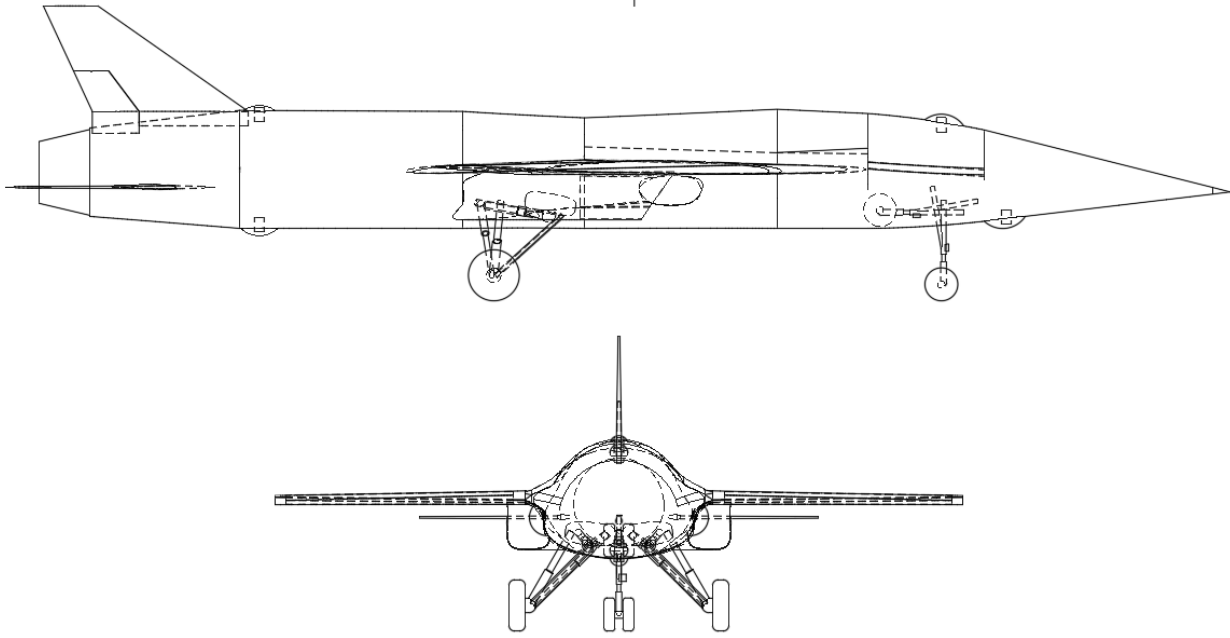


Figure 41: Schemes for retracted and extended configurations of the landing gear

### 13.3 Integration

The landing gear was integrated into the aircraft with the proven oleopneumatic shock strut to effectively dampen hard landings which may be more common as aircraft return from particularly harsh missions. The gear assembly was modeled much like that of the F-16 Fighting Falcon, which has a very compact stowage volume and relatively simple design. The gear retracts into its housing just beneath the aft fuel tank and just forward of the converging section of the engine inlets, as shown in figure 41.

## 14 Design Refinement

The following sections describe changes made to the design in searching for the most optimal option. As a baseline for holistic comparison, figure 42 shows a visual comparison between the preliminary and the final designs.

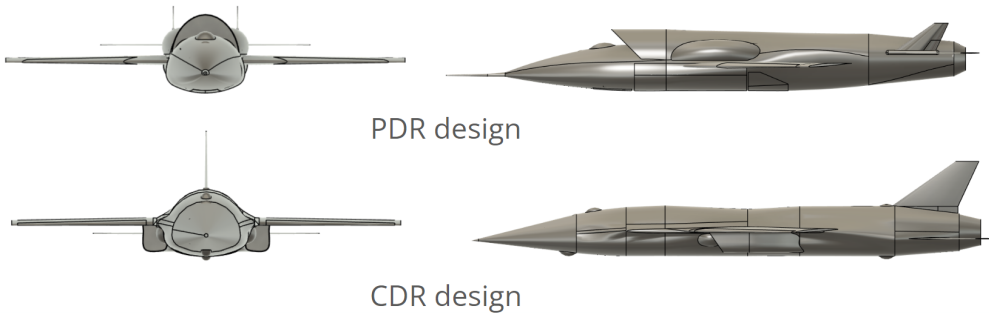


Figure 42: Comparison between preliminary and current designs.

## 14.1 Engine Inlet Design

The fuselage design has undergone several design iterations since our preliminary design. Most prominently, the engine inlet, previously located atop the fuselage, was moved to a more conventional dual under-wing inlets. It was concluded that, without much legacy with regards to the type, and with much more concerns regarding supersonic performance, it would not be optimal to integrate top-mounted inlet technology for our fuselage. This greatly increased the width of the fuselage section, but allocated much more internal storage volume within the aircraft. Although the inlet locations were modified, the diverterless inlet design was retained, as the elimination of complex variable inlet geometry was deemed extremely valuable. The complementing boundary layer diverting shock humps were also retained.

## 14.2 Blended-wing Design

Figure 42 shows a simple connection between the wings and the main fuselage section for the preliminary design, as if the wings were bolted on the sides. There are some benefits to such a design, including ease of manufacturing and lower cost, but the discontinuous nature of the connection gives rise to wave drag beyond transonic speeds, and can become a point of structural failure without a very rigid connection.

Most frontline fighter designs currently in service utilize wing-blending, or the seamless and continuous transition from the fuselage to the wing section; examples include the F-16 Fighting Falcon or the Su-27 Flanker. This not only increases the structural integrity of the entire aircraft, but also contributes to area ruling by allowing a continuous and smooth change in cross-sectional area along the length of the aircraft, decreasing wave drag. To enhance the supersonic performance of the aircraft, wing-blending was actively integrated into the current design, complemented with leading edge extensions to enhance performance in extreme maneuvers.

## 14.3 Internal vs External Carriage

For the Homeland Defense Interceptor (HDI), we selected internal weapons and fuel storage due to the substantial advantages in stealth, aerodynamic performance, and survivability of the aircraft. Internal storage significantly reduces the radar cross-section, making the aircraft less detectable by enemy radar systems. This stealth advantage is critical in ensuring the aircraft can perform its missions undetected, thereby enhancing its effectiveness in homeland defense operations.

Additionally, the reduced aerodynamic drag associated with internal weapons bays and fuel tanks improves the HDI's speed, range, and fuel efficiency, which are vital for extended patrols and quick interception missions. Protection from environmental elements and enemy fire also ensures the reliability and longevity of the weapons. While acknowledging the higher development cost and maintenance complexity, the enhanced aerodynamic performance will result in better operational efficiency and potential cost savings over the aircraft's lifespan. Additionally, we do not expect the cost of implementation to outweigh the benefits and cost-savings down the line. Furthermore, designing for advanced stealth and performance characteristics, the aircraft will remain effective against future and evolving threats, ensuring long-term operational relevance. Ultimately, the benefits in performance, survivability, and long-term operation make internal storage the optimal choice for the design of our aircraft. A summary of the key advantages and disadvantages associated with internal storage is in figure 43.

## 14.4 Missile Reserves

The number of missiles carried by an interceptor is a critical determining factor of a successful mission, in deterring or retaliating against threats. The more missiles an aircraft carries, the more targets it can successfully intercept and neutralize. However, given the decision in the last trade regarding the implementation of an internal weapons bay, the number is limited to how much space can be allocated within the aircraft itself. The aircraft was initially designed to store six AIM-120s, mainly to address the increasing threat of mass-produced UAVs or guided munitions, which can quickly overwhelm an intercepting force without enough firepower. However, not all missions for the interceptor, according to the RFP and also in

Criteria	Internal Storage	External Storage
Radar Cross-Section	Low (better stealth)	High (more detectable)
Aerodynamics	Reduced drag (better performance)	Increased drag (reduced performance)
Survivability	Protected (less vulnerable)	Exposed (more vulnerable)
Development Costs	Higher development cost	Lower development cost
Ease of Maintenance	More difficult to service	Easier to service
Weight distribution	Keeps weight closer to central location of aircraft	Weight stored farther from central location of axis

Figure 43: Trade study to support internal vs external weapons carriage

Criteria	Four Missiles	Six Missiles
Combat Efficiency	Low (less weapons reserve)	High (more weapons reserve)
BVR Performance	Low (can be overwhelmed)	High (can retaliate with ease)
Average Mission Efficiency	Efficient (across all missions)	Inefficient (across all missions)
Sortie Cost	Low (low payload cost)	High (high payload cost)
Complexity	Simple (ample internal volume)	Complex (tight weapons bay)

Figure 44: Trade study to determine number of missiles stored

real applications, involve interception of enemy aircraft. There would be cases in actual deployment where not a single missile could be fired, such as escort missions. Carrying all missiles through all stages of flight would only serve to increase aerodynamic inefficiencies, and jettisoning them would increase the cost. Even if all payload were to be used, this only serves to increase the cost of a single sortie, and increase valuable rearmament and maintenance time. Additionally, the configuration of the pylons used to launch the missiles within the cramped weapons bay would have to be of significant complexity, adding more to maintenance costs and increasing the risk of launch malfunction. As such, it was concluded that a missile store of four AIM-120s would be sufficient for the role of a dedicated interceptor. Indeed, for our fuselage, the maximum non-interfering capacity of missiles (capacity at which no two missiles have interfering maximum fin radii) was exactly four. The trade study matrix in figure 44 summarizes the discussion above.

## 15 Structures

### 15.1 Load Paths

The structural load paths within the aircraft are defined to distribute aerodynamic forces effectively throughout the wing and fuselage.

Figures 45 and 46 show the load distributions of the fuselage and the wing. The fuselage load analysis was necessary to find the fuselage apparent weight which includes the downward tail lift force as well as the fuselage structure, wing structure, tail structure, fuel, payload and engine. This apparent weight correlates to the amount of lifting force acting on the wing and the fuselage loading arrangement was chosen carefully to maintain static stability about the center of gravity.

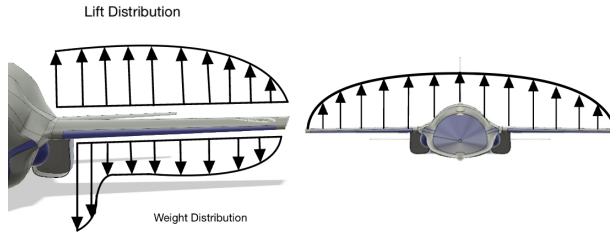


Figure 45: Load Distribution of the Wing

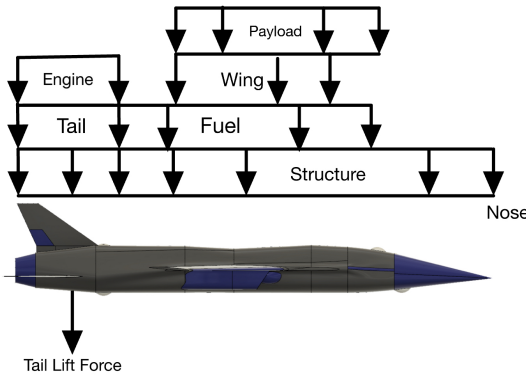


Figure 46: Load Distribution of the Fuselage

The weight distribution along the wing accounts for the internal fuel tanks and its proximity to the fuselage. The weight distribution does not vary greatly since the aircraft does not contain external missile storage which would fluctuate the distributed weight.

On the wing, lift forces are transferred through a multi-spar wing box structure to the fuselage via reinforced ribs and skins. The wingbox is optimized for high-speed maneuvers, and allows for the spars and stringers to reinforce stiffness. On the fuselage, the use of a semi-monocoque structure will ensure longitudinal stiffness. Reinforcements include bulkheads near high-stress zones that eventually carry thrust forces and moments to the wingbox.

### 15.1.1 Distribution of Air Loads on Wing

The air loads on the wings were calculated considering the clean configuration of the aircraft, the dynamic pressure at a specific flight condition ( $q$ ), and the lift coefficient optimized for the clean configuration.

The total lift generated by the wing was calculated as:

$$L = q \times C_L \times S \quad (16)$$

The resulting distributed load ensures sufficient lift for the given flight regime while maintaining structural integrity.

At Mach 1.2 (sea level), the dynamic pressure was calculated as  $q = 2133 \text{ psf}$ , yielding a distributed load of approximately 478,129 lbf over the reference wing area of  $25.25 \text{ m}^2$  ( $271.79 \text{ ft}^2$ ).

A safety factor of 1.5 was applied to account for ultimate load conditions, resulting in a total ultimate load of 717,194 lbf for structural resilience.

## 15.2 V-n Diagrams

The V-n diagrams for the aircraft have been developed for both maximum and minimum weight configurations at 20,000 feet, incorporating gust lines for aerodynamic loading.

The Load Factors associated with our aircraft, laid out in the RFP, are +7 and -3 vertical g's in the clean configuration with 50 percent internal fuel. These maneuver constraints as well as our calculated design airspeeds, laid out in Table 17, permitted the construction of our aircraft's operating envelope.

Design Airspeed	Value(knots)	Symbol
Design Speed at Max Gust	85.1	$V_B$
Design Speed at Normal Cond.	272.6	$V_C$
Design Dive Speed	549.1	$V_D$

Table 17: Design Airspeeds for V-n Diagram

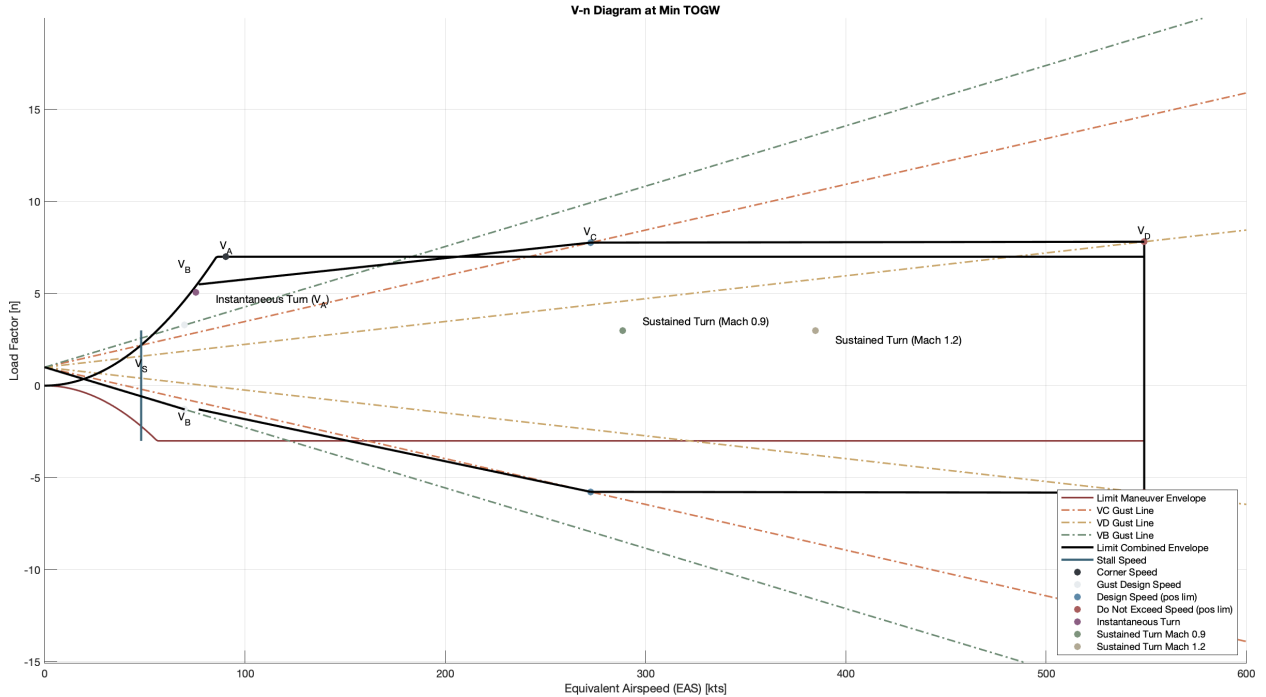


Figure 47: **Maximum Weight V-n Diagram:** This plot shows the operational envelope under the heaviest load conditions, including structural safety limits and stall boundaries.

Figure 47 and 48 shows all of the operating conditions and the combined envelope for a feasibility region regarding our maneuverability and capabilities under certain gust conditions. The instantaneous turn and two sustained turns are all within the feasible region and ensures structural stability at those maneuvers.

### 15.2.1 Maneuverability

Overall, the aircraft's structural layout supports high-speed requirements (up to Mach 1.6) and maneuvers with load factors reaching 5 g's sustained and up to 7.5 g's ultimate. This ensures feasibility and control under these mission-specific turn rates and g-force thresholds.

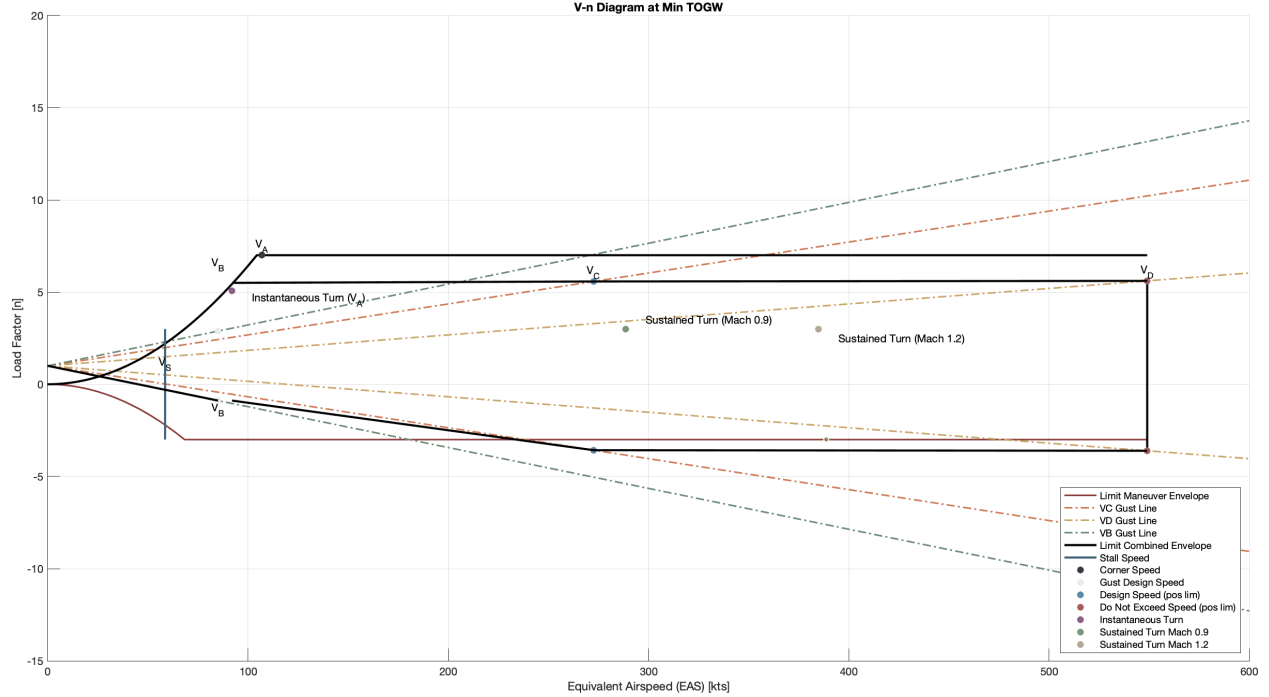


Figure 48: **Minimum Weight V-n Diagram:** This envelope is narrower, with lower structural and aerodynamic constraints due to the reduced inertial load.

## 16 Computational Procedure and Software Design

To assist us in defining design constraints, selecting a design, and optimizing it, we built a comprehensive aircraft sizing software package from the ground up, incorporating methods from Martins [5], Raymer [1], Roskam [19], and other aircraft designers. Our software is implemented entirely in MATLAB due to its compatibility with large, complex, nested data structures and the familiarity of our team with the platform.

Significantly, we decided to utilize structs in MATLAB to store the design parameters in our software. The `aircraft` struct is first initialized in the code with substructs (e.g. `performance`, `mission`, `weight`, `aerodynamics`, etc.), each of which stores related parameters in one centralized location, including both user inputs and values generated by functions. The modular nature of structs allows for easy parametrization of the code. Consequently, we are able to quickly and dynamically re-design our aircraft by changing specific user-inputs, which produces a cascading effect in the rest of our code.

The DSM of our entire software package is pictured in Figure 49 below, displaying a high level overview of the parameters it calculates and how they feed into various functions.

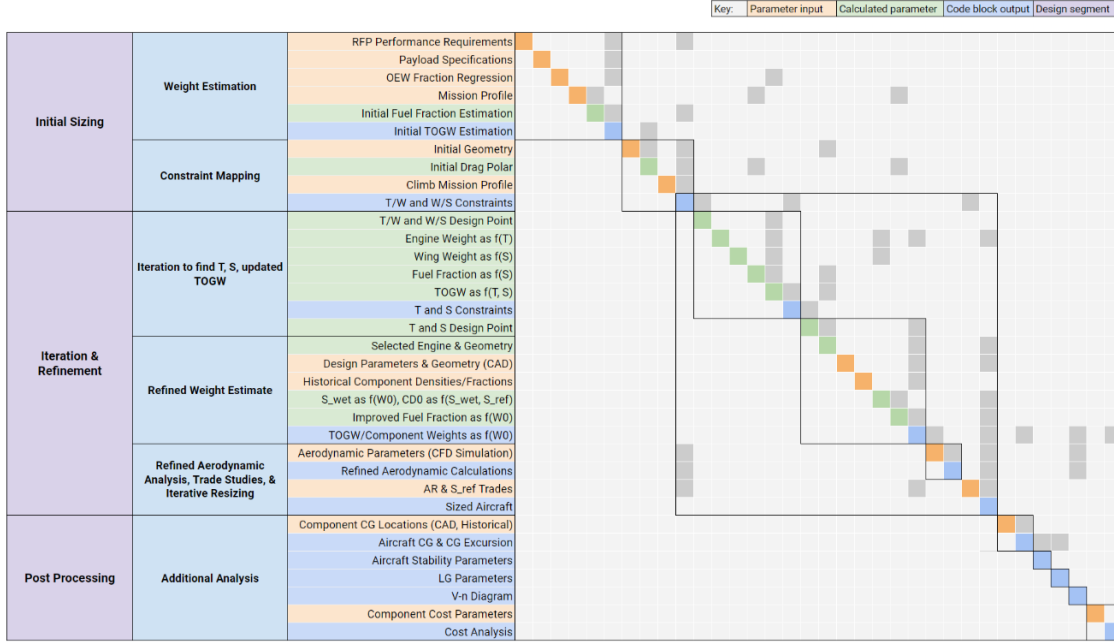


Figure 49: DSM for Libellula's aircraft sizing software

Rows in orange represent user-input values/parameters. Rows in green represent parameters that are calculated and output from a custom-built function. Rows in blue represent parameters that are outputs of code blocks. A block filled in gray above the diagonal indicates an input. For example, *Initial Fuel Fraction Estimation* takes input *Mission Profile*. A block filled in gray below the diagonal indicates an output. For example, the output of *T/W and W/S Constraints* defines *T/W and W/S Design Point*. In the following sections, we will discuss each block in more detail.

## 16.1 Initial Sizing

To begin sizing our aircraft, it was necessary to make a preliminary estimate of our TOGW, which would inform the following design decisions and parameter definitions.

We start by populating our `aircraft` struct with known values. These include performance requirements, payload specifications, and mission profiles indicated by the RFP, in addition to an OEW fraction regression (equation 44), provided as courtesy by collaborating defense contractor Sainristil Defense.

Calculating the fuel fraction was a result of the input mission profile, historical fuel fraction values for specific mission segments, and the Breguet Range Equation. Plugging this fuel fraction (for the DCA mission, the most demanding), our OEW fraction regression, and our payload weight into our TOGW function and iterating, we were able to converge on a preliminary value of TOGW.

Initial geometric parameters were defined, namely the aspect ratio and wing sweep. We were then able to calculate our drag polar, estimating the Oswald efficiency factor  $e$  from Sartorius's MATLAB function [23] which gives  $e$  as a function of wing sweep, aspect ratio and  $C_{D0}$ .  $C_f$ ,  $C_{D0}$  cruise, and  $C_L$  were determined from historical trends for similar aircraft, and  $C_{D0}$  was interpolated for takeoff and landing from delta values given by Roskam Table 3.6 [19].

Using this drag polar and historical values from Roskam [19], we were able to populate our mission struct with parameters for climb. Combining this with our geometric values and drag polar values, we found our *T/W* and *W/S* constraint lines, equations which can be found in section 20.2.

Finding constraint curves was a matter of plugging in an array of *T/W* or *W/S* values into the constraint equations and plotting them over the appropriate regions. From this diagram, a design point was selected manually by observation, at the lowest *T/W* and highest *W/S* value within the feasible region. These plots and the selected design points are shown below. The feasible region is to the left of the landing field line,

and above the specific excess power at 1g, SL line for both max and military thrust.

## 16.2 Finding T, S, and Updated TOGW Estimate

These design points were subsequently used to produce a more refined estimate of TOGW. This new function takes input values of T and S, and has a few key differences from our initial weight estimate. Describing one iteration of a

1. Calculate the empty weight of the aircraft from a guess of TOGW using the regression from Equation 44.

2. Calculate the design parameters:

- $S_{\text{design}} = \text{TOGW} \times (\text{selected design point } T/W \text{ ratio})$
- $T_{\text{design}} = \text{TOGW} \times (\text{selected design point } W/S \text{ ratio})$

3. Adjust the empty weight using the input values of S and T:

- Adjust for wing area:

$$\text{Adjustment for } S = (S_{\text{in}} - S_{\text{design}}) \times (\text{area density of wings})$$

- Adjust for thrust:

$$\text{Engine weight adjustment} = \text{calculate engine weight for } T_{\text{in}} - T_{\text{design}}$$

- Add the engine weight adjustment to the empty weight.

4. Update the empty weight fraction with the new empty weight value.

With our empty weight now calculated, we make a refined estimate of the fuel fraction in a new function:

1. Determine  $S_{\text{wet}}$  using the regression from Equation 45 provided by Roskam Table 3.5 [19].

2. Calculate a new  $C_{D_0}$  using the input  $S_{\text{in}}$ .

3. Use the new  $C_{D_0}$  to determine  $L/D$ .

4. Use the refined  $L/D$  estimate in the Breguet Range equation to find the updated fuel fraction.

With these two fractions and the weight of our payload, we find TOGW and iterate until we converge on a value. This function was validated against the F-35, which we discuss in section 17. Combining our new TOGW estimation with our  $T/W$  and  $W/S$  constraints, we are able to calculate T and S. For example, to calculate T given an value of  $S_{\text{in}}$ :

1. Take a guess of  $T$
2. Calculate TOGW as  $f(T, S)$
3. Calculate  $W/S$  from  $S_{\text{in}}$  and TOGW
4. Calculate  $T/W$  from the constraint equation and the new  $W/S$
5. Calculate the new  $T$  from  $T/W$  and the calculated TOGW
6. Iterate until converged.

The same was repeated to find  $S$  given a value for  $T$  and  $W/S$  constraints. This process was completed for each constraint over defined ranges of  $T$  and  $S$  to find our  $T - S$  plots.

### 16.3 Iteration and Refinement

After selecting  $T$  and  $S$ , we moved forward with selecting the rest of our values for our aircraft design, and began implementing them in CAD. From our CAD model, we were able to find the surface areas of various components. Combining this with historical values for weight densities/TOGW fractions and historical regressions for the aircraft components, we were able to converge on a new estimate for TOGW using the following approach, provided by the metabook [5]:

1. Compute fuel fraction:  $\frac{W_f}{W_0}$
2. Compute fuel weight:  $W_f = \frac{W_f}{W_0} \times W_0$
3. Compute landing gear weight, a fraction of TOGW:  $W_{lg} = 0.043W_0$
4. Compute extra weight, a fraction of TOGW:  $W_{xtra} = 0.17W_0$
5. Compute the new MTOW:

$$W_{0\text{new}} = W_{\text{engine}} + W_{\text{wing}} + W_{\text{ht}} + W_{\text{vt}} + W_{\text{fuse}} + W_{\text{xtra}} + W_{\text{lg}} + W_f + W_{\text{payload}} + W_{\text{crew}}$$

6. Check for convergence
7. Update MTOW value:  $W_0 \leftarrow W_{0\text{new}}$

To calculate fuel fraction for this component weight breakdown, we used an updated method from Cinar [3]. Instead of finding the fuel fraction for cruise in one section, more accuracy can be gained by computed it in segments, accounting for fuel burn in the calculation of the  $L/D$  ratio.

1. Initialize `ff_segments` as an array with size `n`.
2. For each segment `i` from 1 to `n`:
  - (a) Calculate `CL` using current weight and aerodynamic parameters.
  - (b) Calculate `LD` using the lift-to-drag ratio based on `C_L` and `C_D0`.
  - (c) Calculate the fuel fraction for the segment using the Breguet range equation.
  - (d) Update the current weight by multiplying it with the calculated fuel fraction.
3. Find the total fuel fraction for the cruise segment by multiplying each item of `ff_segments`.

Similarly, the fuel fraction for climb can be calculated by segments.

1. Initialize `ff_segments` and `height_energy` as arrays with size `n`.
2. For each segment `i` from 1 to `n`:
  - (a) Determine the value of `C_D0` and `e` based on current altitude `h`.
  - (b) Calculate `k` using `e`.
  - (c) Retrieve air density `rho` at the current altitude `h`.
  - (d) Linearly scale `TSFC` based on altitude.
  - (e) Linearly scale thrust based on air density.
  - (f) Calculate the best velocity for the segment using the equation from Slide 54 [3].
  - (g) Calculate `C_L_i` and `C_D_i` from the lift equation and parabolic drag relation.
  - (h) Calculate drag `D_i`.
  - (i) Calculate the energy height of the segment `h_e(i)`.
  - (j) Calculate fuel fraction from the Breguet range equation: `ff_segments(i)`.

- (k) Update the current weight  $W_i$  based on the fuel fraction.
  - (l) Update altitude  $h$  by adding segment height change.
3. Find the total fuel fraction for the cruise segment by multiplying each item of `ff_segments`.

This component weight breakdown yielded a higher TOGW estimate than the estimate based on T and S. This pushed the aircraft we had initially selected from the  $T - S$  plot to become infeasible. This initiated a series of trade studies between with  $S_{ref}$  (which changes wing loading and TOGW), aspect ratio (which changes TOGW), and airfoil design (to find higher  $C_L$  values, which would loosen specific requirements) to find an aircraft configuration that would provide us a T/W and W/S (using the larger component breakdown TOGW estimate) that would fit into our feasible space. Because of the high parametrization of our code, this only a matter of manually changes values individually until a satisfactory design was found.

## 16.4 Post Processing

Once the aircraft had been sized to meet the given constraints, these aircraft parameters could be fed forward and additional analysis could be conducted. Such items include CG & CG excursion, stability and static margin, landing gear refinement, structural envelope validation and V-n diagram, and a finalized computation of program cost.

## 17 Method Validation

To validate our software, we populated our aircraft struct with parameters that describe the F-35. All values were pulled from the student guide [24]. Most significantly, we defined the crew weight, payload weight, wing loading, and thrust to weight ratio of the F-35, as these are the key values our software uses to calculate the maximum TOGW (MTOW) of the aircraft.

Subsequently, we ran an iteration on our `togw_as_func_of_TS_calc.m` function, which calculates the maximum TOGW of an aircraft given an input wing area and maximum thrust. The input values for this validation are as follows:

Table 18: F-35 Parameters for TOGW Calculation

Parameter	Value
Maximum Thrust, $T$ (N)	190,000
Wing Area, $S$ ( $m^2$ )	42.7
Maximum Takeoff Weight, MTOW (kg)	29,900
Max Thrust-to-Weight Ratio, $T/W$	0.65
Wing Loading, $W/S$ ( $kg/m^2$ )	700

In validating this function, we made one additional key modification. Our software calculates the fuel fraction of the designed aircraft based on the DCA mission provided in the RFP, which is a much more demanding mission with respect to range than the F-35's mission. Consequently, we fixed the fuel fraction in the `togw_as_func_of_TS_calc.m` iteration to 0.28, which is the F-35's fuel mass, 8,300 kg (18,250 lbm) divided by its MTOW. Consequently, we are not validating our fuel fraction function. This is acceptable, as its calculation is specific to our mission alone.

Running our function with these inputs and modifications yields:

Table 19: TOGW Function Validation Summary

Actual Weight (kg)	Calculated Weight (kg)	Percent Difference (%)
29,900	31,900	6.69

We deem our percent error, 6.69%, to be sufficiently low for our preliminary weight estimations. When plotting the F-35 design points on our  $T/W - W/S$  and  $T - S$  plots, the point does not fall within our feasible region. This is expected, as the F-35 does not have the same constraints that our aircraft does. These constraints are not readily available online, but can be roughly solved for given the F-35's specifications.

## 18 Conclusions

The Libellula F-81 aircraft design successfully meets all the primary mission and performance requirements set forth during its conceptualization. Its advanced systems and robust design choices have ensured it is fully capable of performing in the demanding environments for which it was designed. From subsonic cruise capabilities to its superior combat maneuverability, the F-81 embodies balance between innovation and affordable functionality. The inclusion of advanced avionics, redundant systems, and highly reliable sensor arrays further confirms that the aircraft design effectively address the operational needs of a remotely-piloted homeland defense interceptor.

Despite the success of the current design, there are areas identified for further refinement to optimize performance and improve system integration. One key area is the analysis of the aircraft's truly optimal cruising speed and altitude. Additionally, a more precise drag analysis is needed to fine-tune the aircraft's drag coefficient estimate. By incorporating updated drag data into the performance constraints and iteratively resizing the design, the F-81 can achieve an even higher degree of aerodynamic efficiency.

Another area for refinement involves the internal configuration of components relative to the center of gravity (CG). To better meet stability margin (SM) requirements, shifting certain components closer to the CG would improve the overall balance of the aircraft and potentially reduce trim drag. This adjustment would enhance handling characteristics, particularly during high-angle-of-attack scenarios or abrupt maneuvers, and would ensure less CG travel over the flight envelope and stay within the 10% to -10% range required by the RFP.

In conclusion, while the Libellula F-81 is already a highly capable and mission-ready aircraft, addressing these open items would further refine its performance, efficiency, and stability. These adjustments will ensure that the design not only meets but exceeds operational expectations, solidifying its role as a leading-edge solution in modern aerial combat and reconnaissance missions.

## 19 References

- [1] Raymer, D. P., *Aircraft Design: A Conceptual Approach*, AIAA Education Series, American Institute of Aeronautics and Astronautics, Inc., Reston, VA, 2018.
- [2] Lutze, “AOE 3104 Course Materials,” Accessed: 2024-10-27.
- [3] Çınar, G., “Lecture 13 - Sizing Refinement,” Oct. 2024, October 28, 2024.
- [4] contributors, W., “General Electric F110 – Wikipedia, The Free Encyclopedia,” [https://en.wikipedia.org/wiki/General\\_Electric\\_F110](https://en.wikipedia.org/wiki/General_Electric_F110), 2024, Accessed: 2024-12-08.
- [5] Martins, J. R. R. A., *The Metabook of Aircraft Design*, 2021, Compiled on Sunday 17<sup>th</sup> October, 2021 at 06:26.
- [6] Roskam, J., *Airplane Design: Part V - Component Weight Estimation*, Roskam Aviation and Engineering Corporation, Ottawa, Kansas, 1985, First Printing.
- [7] Finck, R. D., *United States Air Force Stability and Control DATCOM*, McDonnell Douglas Corporation, 1978, Accessed: 2024-10-25.
- [8] Gilruth, R. R., “Analysis and prediction of longitudinal stability of airplanes,” Tech. rep., NACA, 1941, Accessed: 2024-10-25.
- [9] Force, U. A., “F-16 Fighting Falcon,” n.d.
- [10] Vietnam Warbirds Resource Group, “Lockheed F-104 Starfighter,” 2024, Accessed: 2024-10-24.
- [11] Güzelbey, H., Eraslan, Y., and Doğru, M. H., “Effects of Taper Ratio on Aircraft Wing Aerodynamic Parameters: A Comparative Study,” *European Mechanical Science*, Vol. 3, No. 1, 2019, pp. 18–23, Accessed: 2024-10-24.
- [12] Scholz, D., “Aircraft Design - Part VII: Wing Design,” 2021, Accessed: 2024-10-24.
- [13] Unknown, A., “Title Unknown,” *Munin Open Research Archive*, Year Unknown, Accessed: 2024-10-24.
- [14] Embry-Riddle Aeronautical University, “Flying Fast,” 2024, Accessed: 2024-10-24.
- [15] Embry-Riddle Aeronautical University, “Anatomy of Aircraft and Spacecraft,” 2024, Accessed: 2024-10-24.
- [16] Hosseini, S. A., Shakiba-Hojjati, M., Ghiasi, H., and Khalkhali, A., “Aerodynamic Design and Analysis of Winglets,” 2012, Accessed: 2024-10-24.
- [17] Kasi, L. and Thangavelu, P., “Reducing Shock Wave Strength on Airfoil Surfaces with Nanomaterial Coating at Supersonic Speed,” 2024, Accessed: 2024-10-24.
- [18] Spreemann, K. P., “Technical Memorandum: NASA-TM-X-26,” Technical Memorandum (TM) NASA-TM-X-26, NASA Langley Research Center, Hampton, VA, United States, aug 1959, Document ID: 19630003100, Acquisition Source: Langley Research Center, Accession Number: 63N12976.
- [19] Roskam, J., *Airplane Design: Preliminary Sizing of Airplanes*, Roskam Aviation and Engineering Corporation, Ottawa, Kansas, 1985, First printing.
- [20] News, G. A., “GE Launches F110 Fighter Engine Variant With 400MillionWinAtUnitedArabEmirates,” 2023, Accessed : 2024 – 12 – 08.

- [21] Roskam, J., *Airplane Design: Part VIII: Airplane Cost Estimation: Design, Development, Manufacturing and Operating*, Roskam Aviation and Engineering Corporation, Ottawa, Kansas, USA, 1990, First Printing (hardbound).
- [22] Eastwood, B. M., “The F-22 Raptor Stealth Fighter Is Worth Every Penny,” *The National Interest*, November 2023, Accessed: 2024-12-08.
- [23] S., S., “Oswald efficiency estimation function,” <https://www.mathworks.com/matlabcentral/fileexchange/38800-oswald-efficiency-estimation-function>, 2024, MATLAB Central File Exchange, Retrieved October 23, 2024.
- [24] Cinar, G., “AE481 Aircraft Design: Syllabus and Guide,” Compiled on Tuesday 10th September, 2024 at 15:35 UTC, 2024.
- [25] Hosseini, E., “CFD analysis of the aerodynamic characteristics of biconvex airfoil at compressible and high Mach numbers flow,” *SN Applied Sciences*, Vol. 1, 2019, pp. 1283.
- [26] Scholz, D., “Aircraft Design for HOOU,” <https://www.fzt.haw-hamburg.de/pers/Scholz/HOOU/index.html>, 2024, Open Educational Resource (OER) from Hamburg Open Online University.
- [27] Force, U. A., “F-35A Lightning II,” n.d.
- [28] Force, U. A., “F-22 Raptor,” n.d.
- [29] Tan, H., G. R., “Design and Wind Tunnel Study of a Top-mounted Diverterless Inlet,” *Chinese Journal of Aeronautics*, Vol. 17, 2004, pp. 72–78.
- [30] Ge, C., S. Y. X. L., “Design and Analysis of a Ventral Diverterless Supersonic Inlet,” *Journal of Physics: Conference Series*, Vol. 1985, 2021.
- [31] McGhee, R. J. and Beasley, W. D., “Low-Speed Aerodynamic Characteristics of a 17-Percent-Thick Supercritical Airfoil Design for General Aviation Applications,” Tech. Rep. NASA-TP-1538, NASA Langley Research Center, 1979, Accessed: 2024-10-24.
- [32] Global Aircraft Organization, “J-7 Fishbed,” 2024, Accessed: 2024-10-24.

## 20 Appendix

### 20.1 Cost

#### 20.1.1 Adjusting for Inflation

$$b_{\text{CEF}} = 5.17053 + 0.104981 \cdot (1989 - 2006) \quad (\text{Base year CEF}) \quad (17)$$

$$t_{\text{CEF}} = 5.17053 + 0.104981 \cdot (2024 - 2006) \quad (\text{Target year CEF}) \quad (18)$$

$$\text{cost}_{2024} = \text{cost}_{1989} \cdot \frac{t_{\text{CEF}}}{b_{\text{CEF}}} \quad (\text{Adjusted cost}) \quad (19)$$

#### 20.1.2 95% Learning Curve Correction

From Raymer 18.4.1 [1]:

$$H_{\text{adj.}} = H_1 \cdot \left( \frac{1}{Q} \right)^{1-x} \quad (20)$$

Where  $x = 0.926$  for a 95% learning curve,  $H_1$  is the number of hours to produce the first aircraft, and  $Q$  is the number of aircraft produced.

### 20.2 Constraint Equations

#### 20.2.1 $\frac{W}{S}$ Constraint from Landing Field Length

Gathered from Scholz, Section 5 Eqn. 5.5 [26]

$$\frac{m_{ML}}{S_W} = k_L \cdot \sigma \cdot C_{L,\max,L} \cdot (s_{\text{runway}} - s_a) \quad (21)$$

with  $k_L = 0.107 \text{ kg/m}^3$ .  $s_{\text{runway}} = 8000 \text{ ft}$   $s_a = 1000 \text{ ft}$   $\sigma = \frac{\rho_{\text{SL, } 30^\circ\text{C}}}{\rho_{\text{MSL}}}$

#### 20.2.2 $\frac{T}{W}$ Takeoff Field Length

From Roskam Section 3.9 [19]

$$\frac{T}{W} = \frac{1}{k_2} \left( \frac{k_1 \cdot \frac{W}{S} \text{ in} + \text{BFL} \cdot \rho_{\text{SL, } 30^\circ\text{C}} \cdot 0.72 \cdot C_{D0,\text{TO}}}{\text{BFL} \cdot \rho_{\text{SL, } 30^\circ\text{C}} \cdot C_{L,\max, \text{ TO}}} + \mu_G \right) \quad (22)$$

with  $BFL = 8000 \text{ ft}$   $k_1 = 0.0447$   $k_2 = 0.76$   $\mu_G = 0.03$   $C_{L,\text{TO}} = 1.7$

#### 20.2.3 $\frac{W}{S}$ Instantaneous Turn

From Raymer Section 5.3.9 [1]

$$n = \sqrt{\left( \frac{\psi V_{\text{corner}}}{g} \right)^2 + 1}, \quad (23)$$

$$q = \frac{\rho_{35000 \text{ ft}} \cdot (V_{\text{corner}})^2}{2} \quad (24)$$

$$\frac{W}{S} = \frac{q \cdot C_{L,\text{combat}}}{n} \quad (25)$$

$v_{\text{corner}} = 155.556 \text{ m/s}$  (550 km/hr)  $\psi = 18\text{deg/s}$  (from RFP)

#### 20.2.4 $\frac{T}{W}$ Sustained Turn

From Raymer Section 5.3.9 [1]

$$n = \frac{1}{\cos(\theta_{\text{bank}})} \quad (26)$$

$$q = \frac{\rho_{35000\text{ft}} \cdot v_{\text{turn}}^2}{2} \quad (27)$$

$$T_W = \frac{q \cdot CD_0^{\text{clean}}}{\frac{W}{S} \cdot g} + \frac{n^2}{q \cdot \pi \cdot AR \cdot e_{\text{combat}}} \cdot \left( \frac{W}{S} \cdot g \right) \quad (28)$$

#### 20.2.5 $\frac{T}{W}$ Cruise and Dash

From Aircraft Design Metabook Chapter 4.10 [5]

$$n = 1 \quad (29)$$

$$q_{\text{cruise}} = \frac{\rho_{35000\text{ft}} \cdot v_{\text{cruise}}^2}{2} \quad (30)$$

$$\frac{T}{W_{\text{cruise}}} = \frac{q_{\text{cruise}} \cdot CD_0^{\text{clean}}}{\frac{W}{S} \cdot g} + \frac{n^2}{q \cdot \pi \cdot AR \cdot e_{\text{cruise}}} \cdot \left( \frac{W}{S} \cdot g \right) \quad (31)$$

$$q_{\text{dash}} = \frac{\rho_{35000\text{ft}} \cdot v_{\text{dash}}^2}{2} \quad (32)$$

$$\frac{T}{W_{\text{dash}}} = \frac{q_{\text{dash}} \cdot CD_0^{\text{clean}}}{\frac{W}{S} \cdot g} + \frac{n^2}{q \cdot \pi \cdot AR \cdot e_{\text{supersonic}}} \cdot \left( \frac{W}{S} \cdot g \right) \quad (33)$$

#### 20.2.6 $\frac{T}{W}$ Ceiling

From Aircraft Design Metabook Chapter 4.11 [[5]]

$$T_W = \left( \frac{\rho_c}{\rho_{SL}} \right)^{0.6} \cdot T_{SLS} \quad (34)$$

$$\frac{T}{W} = \frac{1}{\left( \frac{\rho_c}{\rho_{SL}} \right)^{0.6}} \cdot \left( G + 2\sqrt{\frac{C_{D0}}{\pi A Re}} \right) \quad (35)$$

#### 20.2.7 $\frac{T}{W}$ Climb

From Aircraft Design Metabook Chapter 4.7 [5]

$$\frac{T}{W} = \frac{(K_s)^2}{C_{L,\text{max}}} \cdot C_{D0} + \frac{C_{L,\text{max}}}{(K_s)^2 A Re} + G \quad (36)$$

$$\left( \frac{T}{W} \right)_{\text{takeoff}} = \left( \frac{1}{0.8} \right) \cdot \left( \frac{1}{0.94} \cdot \left( \frac{N_{\text{engine}}}{N_{\text{engine}} - 1} \right) \cdot \left( \frac{W}{W_{\text{takeoff}}} \right) \cdot \left( \frac{T}{W} \right) \right) \quad (37)$$

### 20.2.8 $\frac{T}{W}$ Specific Excess Power

From Raymer Textbook Chapter 7 [1]

$$P_{SE} = \frac{T - D}{W} \cdot V \quad (38)$$

$$\frac{W}{S}_{50\%fuel} = \frac{W}{S}_{N/m^2} \frac{(1 + (1 - ff))}{2} \cdot n \quad (39)$$

$$q_{dash} = \frac{\rho \cdot v^2}{2} \quad (40)$$

$$C_L = \frac{\frac{W}{S}_{50\%fuel}}{q} \quad (41)$$

$$C_D = C_{D_0} + \frac{C_L^2}{\pi \cdot AR \cdot e} \quad (42)$$

$$\frac{T}{W}_{SEP} = \frac{P_s}{v} + \frac{qC_D}{\frac{W}{S}_{50\%fuel}} \quad (43)$$

## 20.3 Additional Equations

### 20.3.1 Empty Weight Fraction Regression

$$\frac{W_e}{W_0} = 0.882 \cdot W_0^{-0.055} (\text{lbm}) \quad (44)$$

### 20.3.2 $S_{wet}$ from TOGW Regression

$$S_{wet} (\text{ft})^2 = 10^{-0.1289} \cdot W_0^{0.7506} \quad (45)$$

## 20.4 Additional Plots

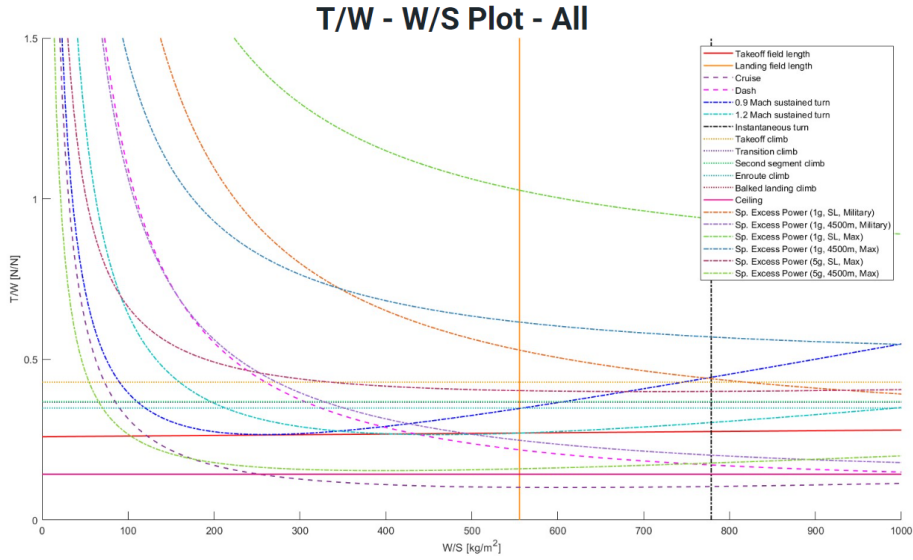


Figure 50:  $T/W - W/S$  Plot, All Constraints Together

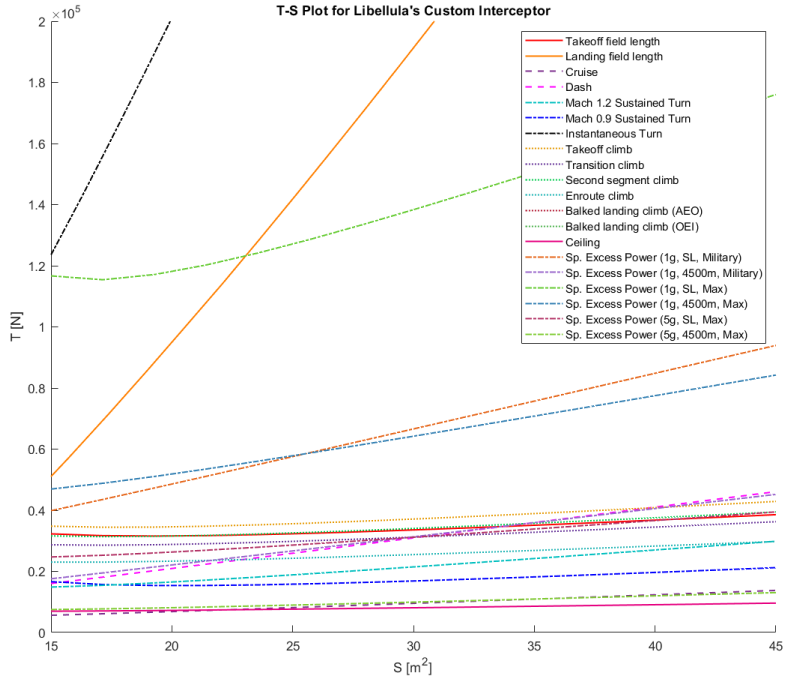


Figure 51:  $T - S$  Plot, all constraints

## 20.5 Wing Parameters

$$\Delta C_{D_{0\text{flap}}} = F_{\text{flap}}(C_f/C)(S_{\text{flapped}}/S_{\text{ref}})(\delta_{\text{flap}} - 10) \quad (12.61)$$

where

$\delta_{\text{flap}}$  = in degrees

$F_{\text{flap}}$  = 0.0144 for plain flaps = 0.0074 for slotted flaps

$C_f$  = chord length of flap (see Fig. 12.18)

$$\Delta C_{D_i} = k_f^2(\Delta C_{L\text{flap}})^2 \cos \Lambda_{\bar{c}/4} \quad (12.62)$$

Figure 52: Equations From Raymer Used for Flap Sizing

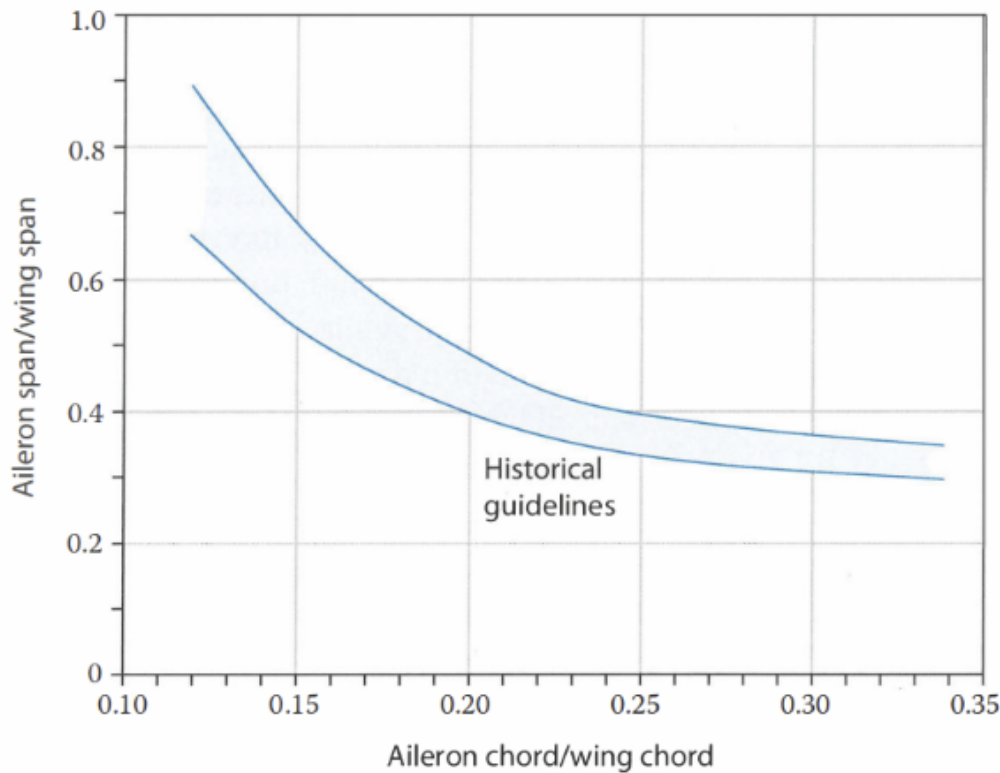


Figure 53: Chart in Raymer Used for Aileron Sizing

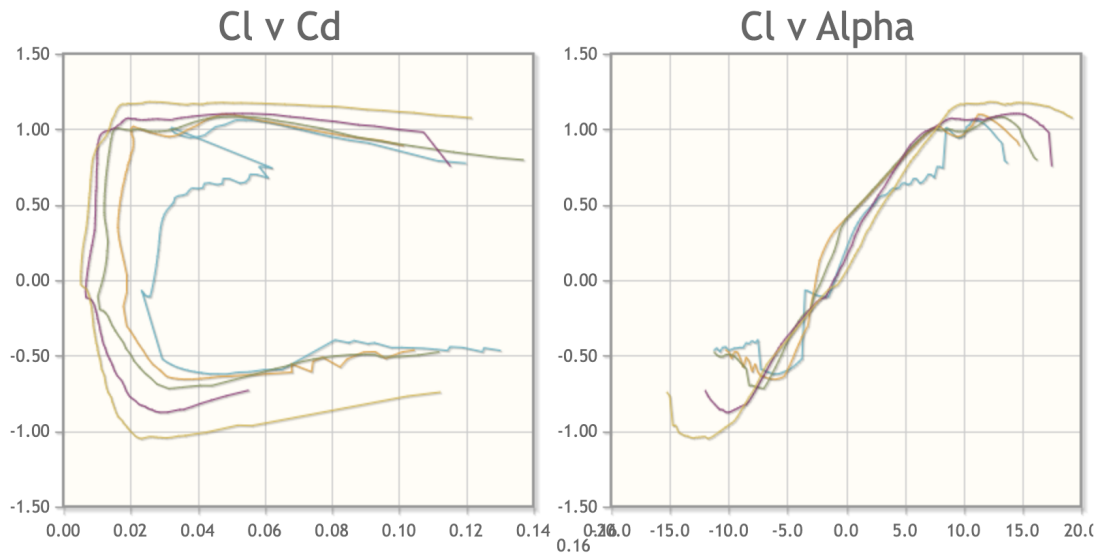


Figure 54: Drag Polar and Cl Alpha Graph for the TsAGI S-12 Airfoil

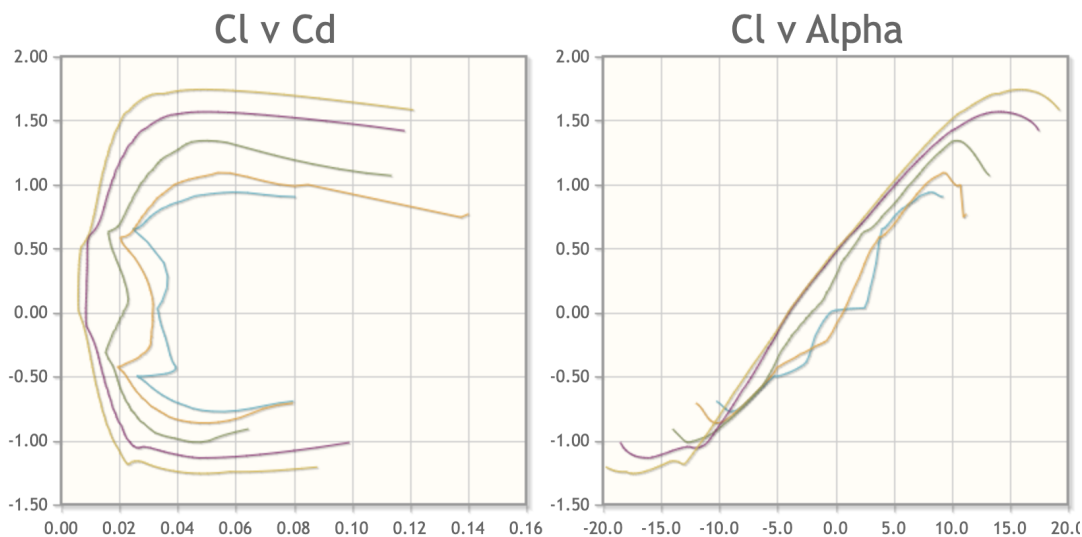


Figure 55: Drag Polar and Cl Alpha Graph for the NASA SC(2)-0.614 Airfoil

## 20.6 Wing Design

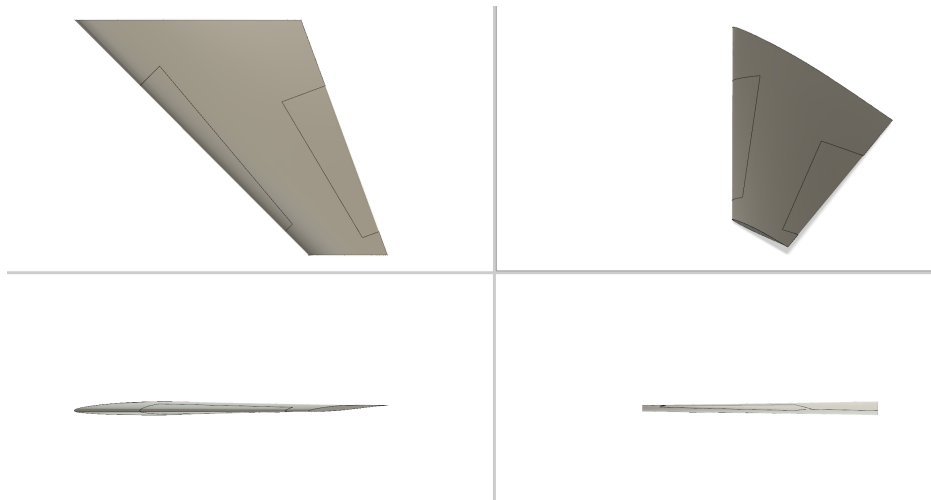


Figure 56: 4-View CAD of Wing Design

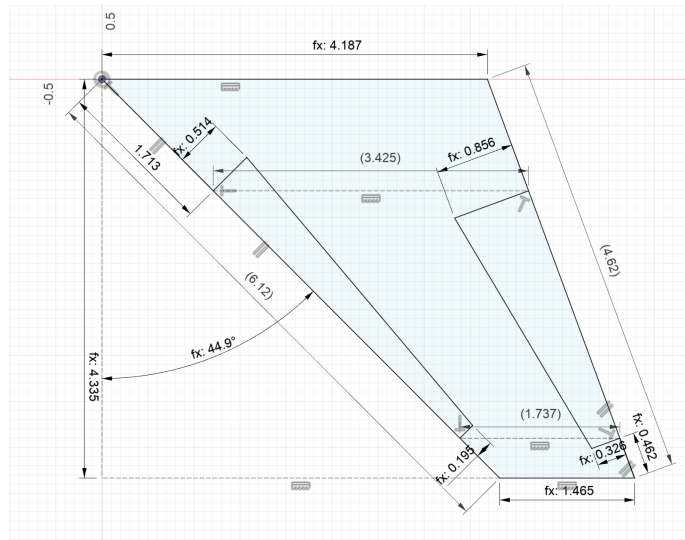


Figure 57: Top-View of Wing Design with Labeled Dimensions and Parameters

Table 20: Values of  $e$  for Different Aircraft Configurations

Configuration	$e$
Cruise	0.881
Takeoff Flaps	0.853
Landing Flaps	0.747
Supersonic	0.500

Table 21: Values of  $C_{D_0}$  for Different Aircraft Configurations

Configuration	$C_{D_0}$
Clean	0.024
Takeoff Flaps	0.034
Takeoff Flaps + Gear	0.049
Landing Flaps	0.079
Landing Flaps + Gear	0.094

Table 22: Values of  $C_L$  for Different Aircraft Configurations

Configuration	$C_L$
Cruise	1.25
Takeoff Flaps	1.70
Landing Flaps	2.00
Combat	1.00

Table 23: Values of  $C_D$  for Different Aircraft Configurations

Configuration	$C_D$
Cruise	0.208
Takeoff Flaps	0.385
Takeoff Flaps + Gear	0.400
Landing Flaps	0.634
Landing Flaps + Gear	0.649

Table 24: Values of  $L/D$  for Different Aircraft Configurations

Configuration	$L/D$
Max Cruise	9.46
Cruise	6.02
Max Takeoff Flaps	7.82
Takeoff Flaps	4.42
Max Takeoff Flaps + Gear	6.50
Takeoff Flaps + Gear	4.25
Max Landing Flaps	4.79
Landing Flaps	3.15
Max Landing Flaps + Gear	4.39
Landing Flaps + Gear	3.08

Table 25: Values of Air Density ( $\rho$ ) for Different Conditions

Condition	$\rho$ (kg/m <sup>3</sup> )
SL at 30°C	1.164
35,000 ft	0.379
MSL	1.088

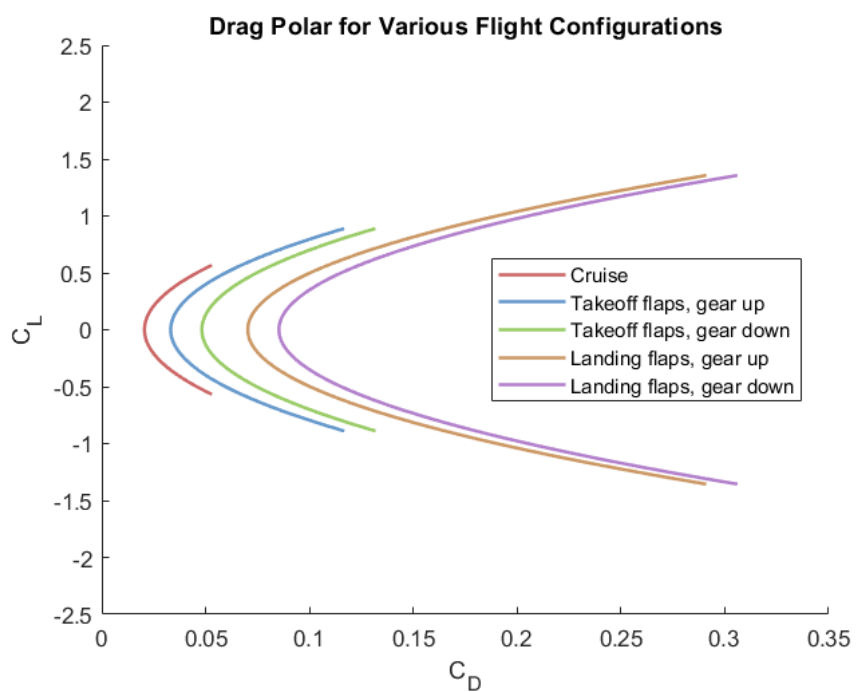


Figure 58: Preliminary Drag Polar for Our Aircraft

## 20.7 Empennage Design

Table 26: Summarized Empennage Parameters

Parameter	Vertical Tail	Horizontal Tail
Single Surface Reference Area	$0.8695 \text{ m}^2$	$1.8303 \text{ m}^2$
Single Surface Span	0.9325 m	1.9133 m
Root Chord	1.3815 m	1.2755 m
Tip Chord	0.4835 m	0.6378 m
Aspect Ratio	2	4
Sweep ( $\Lambda$ )	$55^\circ$	$49.9^\circ$
Taper ( $\lambda$ )	0.35	0.5
Airfoil Shape	Biconvex	Custom
Max Thickness to Chord Ratio ( $\frac{t}{c_{max}}$ )	3.3%	3.3%
Location of $\frac{t}{c_{max}}$	$0.5c$	$0.5c$
Low Speed Lift Curve Slope ( $\frac{\partial C_L}{\partial \alpha}$ )	$0.067 \text{ rad}^{-1}$	$0.067 \text{ rad}^{-1}$
Transonic Lift Curve Slope ( $\frac{\partial C_L}{\partial \alpha}$ )	$0.077 \text{ rad}^{-1}$	$0.077 \text{ rad}^{-1}$
Supersonic Lift Curve Slope ( $\frac{\partial C_L}{\partial \alpha}$ )	$0.073 \text{ rad}^{-1}$	$0.073 \text{ rad}^{-1}$
Incidence Angle	-	-

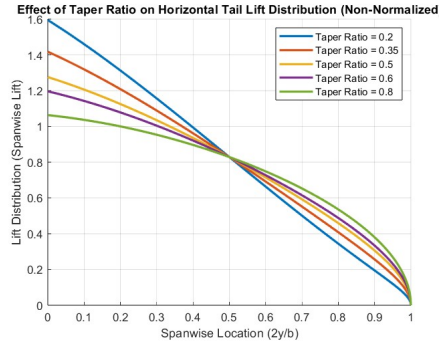


Figure 59: Non-Normalized Lift Distribution on Horizontal Tail with Varying Taper Ratios

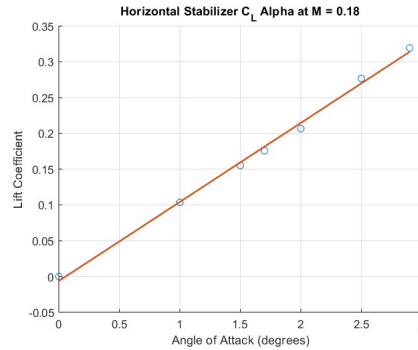


Figure 60: Lift Curve Slope from NACA 0003 mfoil Simulations at Take-Off Mach

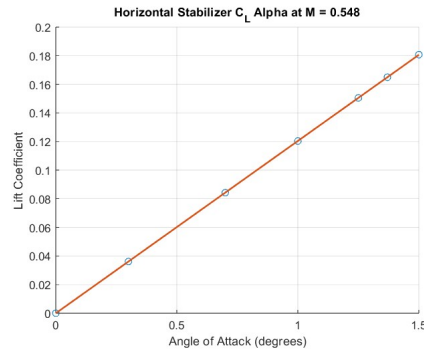


Figure 61: Lift Curve Slope from NACA 0003 mfoil Simulations at Cruise Mach

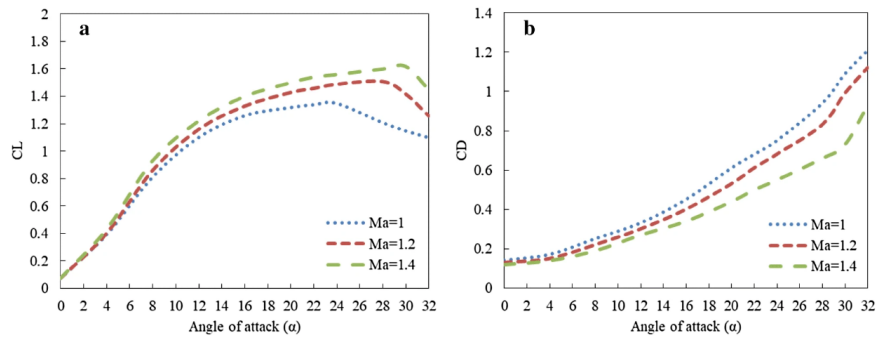


Figure 62: Lift Curve Slope from Biconvex Airfoil CFD Simulations Performed by Hosseini [25]

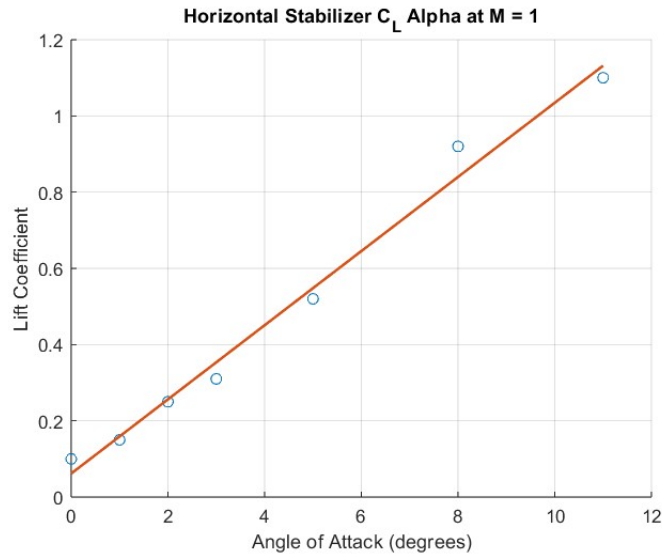


Figure 63: Lift Curve Slope Regression from Hoseini [25] CFD Data Linear Segment at  $M = 1$

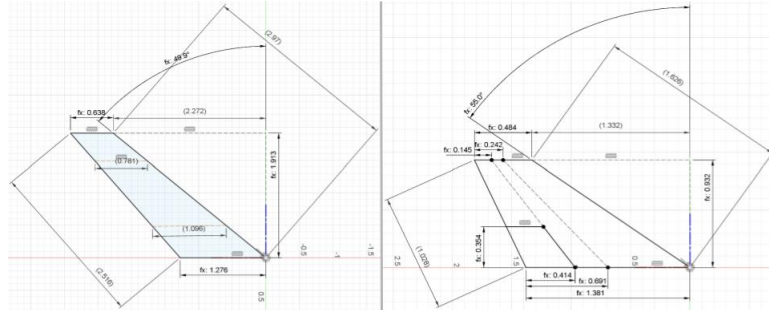


Figure 64: Horizontal Tail [Left] and Vertical Tail [Right] Dimensions



Figure 65: Horizontal Tail [Left] and Vertical Tail [Right] 3D Render